Gong, N., Freddi, F., Li, P. (2024). Shaking table tests and numerical analysis of RC coupled shear wall structure with hybrid replaceable coupling beams. Earthquake Engineering & Structural Dynamics. DOI: 10.1002/eqe.4088.

# Shaking table tests and numerical analysis of RC coupled shear wall structure with hybrid replaceable coupling beams

**Nan Gong**[1], **Fabio Freddi**[2], **Peizhen Li**[1,*]

[1] *State Key Laboratory of Disaster Reduction in Civil Engineering, Tongji University, Shanghai 200092, China*
[2] *Dept. of Civil, Environmental & Geomatic Engineering, University College London, London WC1E 6BT, UK*
[*] Corresponding Author. Tel.: +86 (021) 65983707. E-mail address: lipeizh@tongji.edu.cn

## Abstract

A variety of innovative structural solutions have been recently introduced to mitigate damage and expedite the repair of buildings subjected to extreme seismic events, hence contributing to the urgent need for resilient societies. In this context, the present study experimentally and numerically investigates an innovative reinforced concrete (RC) shear wall (SW) structure with replaceable coupling beams equipped with hybrid devices. These hybrid devices couple metallic and viscoelastic dampers and aim at satisfying multiple lateral load performances effectively. To assess the seismic performance of the proposed coupled SW system and verify the design principle, comparative shaking table tests were performed on two 1/4-scale seven-story SW structure specimens, including a conventional RC coupled SW and the proposed coupled SW with hybrid devices. The tests results indicate the improved performance of the proposed compared with the conventional system in terms of: *1)* reduced interstory drifts and story accelerations demand under a wide range of seismic intensities, *2)* concentrated damage in the hybrid device and minimal damage to the other components contributing to the reparability of the structure. Furthermore, 3D finite element models for the shaking table test specimens were established in OpenSees and validated against experimental response. Successively, a numerical parametric study was conducted by performing non-linear response history analyses under a set of 22 ground motions to investigate the influence of different design configurations of the hybrid device on the peak interstory drifts and peak story accelerations.

**Keywords**: *Coupled shear wall structure; Replaceable coupling beams; Hybrid devices; Earthquake resilience; Shaking table test; Numerical simulation.*

## 1. INTRODUCTION

Seismic design methods, suggested by most current codes and guidelines [1-3] and conventionally applied worldwide, are based on energy dissipation related to structural damage to prevent collapse during extreme seismic events. Although this design approach allows meeting the life safety requirements, it often leads to significant direct and indirect losses, strongly affecting the overall resilience of communities, especially when the damaged structures include strategic facilities, such as hospitals, fire stations, etc., that must remain operational in the aftermath of a damaging earthquake.

In contrast, innovative technologies such as energy dissipation devices offer the opportunity to preserve structural and non-structural components from damage. Moreover, dissipative devices can be used as structural fuses to concentrate damage so that they can be easily replaced, and structures can return to a fully functional condition within a relatively short time interval after the earthquake, hence promoting seismic resilience [4,5]. In this context, several innovative construction technologies (*e.g.*, supplemental damping devices [6-8], structural fuses [9], seismic isolation systems [10,11], rocking [12-14], and self-centering systems [15-18]) have been proposed in recent years for the development of seismic-resilient structures, hence minimizing the consequences of extreme seismic events.

Of particular interest is the use of dissipative devices within high-rise buildings. High-rise structures in seismic-prone regions are often based on reinforced concrete (RC) shear walls (SWs) with coupling beams (CBs) [19,20]. These structures benefit from the superior lateral stiffness of the RC SWs, with the CBs reducing the moment demand at the base of the SWs and acting as fuses to dissipate the seismic energy by undergoing plastic deformations (*i.e.*, damage). However, damaged CBs can be difficult to repair, often leading to construction demolition (*e.g.*, the 2008 Wenchuan [21], 2010 Chile [22,23], and 2011 Christchurch [24,25] earthquakes highlighted the extensive damage at the base of SWs and in the CBs).

To address this issue, several recent studies proposed and developed innovative replaceable coupling beams (RCBs) incorporating dissipative seismic devices. Fortney *et al.* [26] first proposed the use of RCBs composed of steel beams encased within the SWs and bolted yielding components placed in the central part of the RCBs. The design of this system aims at limiting the plastic deformations to the central part of the CBs, while the SWs and the connection between CBs and SWs are kept intact. Additional RCBs have been successively developed, including the use of displacement-dependent devices (*i.e.*, metallic and friction devices) and velocity-dependent devices (*i.e.*, viscoelastic devices). Metallic and friction devices are typically characterized by high stiffness, high strength, and stable energy dissipation capacity and have been incorporated into RCBs in different configurations. Metallic devices dissipate seismic energy through plastic deformations and have been developed in different forms, including conventional I-shaped links [27], steel plate dampers with strip holes [28], and I-shaped steel CBs with diamond-shaped holes in the web [9,29]. Friction devices dissipate seismic energy through relative displacements of steel plates clamped together by post-tensioned bolts passing through slotted

holes to enable the sliding of the plates in contact. A friction material with a large and stable friction coefficient under cyclic loading is typically used at the interface. The sliding force is controlled by the friction material's properties and by the bolts' post-tensioned force [30-32]. Conversely, viscoelastic devices [33,34] are often based on layers of High-Damping Rubber (HDR) materials [35] bonded between steel plates and subjected to shear deformations. Unlike metallic and friction devices, these systems are characterized by lower stiffness and dissipation capacity but have the advantage of dissipating energy even for small deformations. Several applications of RCBs implementing metallic, friction, or viscoelastic devices exist in literature. However, in most of these studies, these devices are used independently, while only a limited number of research works focused on the potential benefits deriving from their combination.

When used independently, these devices typically do not allow satisfying multiple lateral load performances effectively, and this limitation is particularly relevant for high-rise buildings. While in low-rise buildings, the seismic load is usually predominant, in high-rise buildings, seismic and wind loads could be equally important, and both actions could significantly affect the design of the horizontal resisting system. Wind loads could generate significant amplitude vibrations and resonant responses due to the low natural frequencies and low damping of the structure [36], and in some cases, these vibrations can reach beyond the occupants' comfort [37] and induce fatigue damage in the structure [38]. On the other end, high-intensity seismic events could generate extensive damage to the structures and lead to collapse.

Metallic and friction devices are typically designed to remain elastic under wind load (*e.g.*, provide stiffness without energy dissipation) and hence do not contribute to meeting the comfort requirements of high-rise structures. At the same time, they provide better performances under high-intensity earthquakes (*i.e.*, wider hysteretic loops - higher energy dissipation). Conversely, viscoelastic devices provide energy dissipation capacity under small vibrations but typically do not perform well under high-intensity earthquakes due to their limited maximum damping force and relatively small lateral stiffness.

To address this issue, a limited number of research studies, mostly numerical, focused on developing and investigating hybrid systems deriving from the combination of the previously mentioned devices. Ibrahim *et al.* [39] proposed a visco-plastic device consisting of a block of high-damping viscoelastic material sandwiched between two steel shapes (plates or channels). Karavasilis *et al.* [40] numerically investigated a combination of viscoelastic and self-centering devices arranged in series. Vargas and Bruneau [41] investigated the effects of metallic and fluid viscous dampers arranged in parallel. Marshall *et al.* [42] studied several possible combinations of HDR or fluid viscous dampers and buckling-restrained braces (BRBs) working in series or in parallel. More recently, Rahnavard *et al.*[43] proposed a hybrid damper system combining a steel U-shaped damper and a rubber core. The numerical results showed the beneficial effects of these systems in terms of increased energy dissipation and effectiveness in reducing the structural response across a wider range of vibration frequencies and intensities. Only a few studies experimentally investigated similar hybrid devices. Some relevant examples include the work from Marshall and Charley [44,45], which developed and tested a hybrid passive control device consisting of a HDR-based damper connected in series with a BRB. The experimental results showed that the viscoelastic element could be activated for vibration amplitudes significantly smaller than those required to reach the BRB damper yield force. A similar concept was used in Yamamoto and Sone [46]. Recently, Benavent-Climent *et al.* [47] proposed and experimentally investigated through shaking table tests a new hybrid device combining in parallel a low-cost viscoelastic and a yielding metallic component.

However, although some advancements have been made in this direction, only a few studies focused on hybrid devices for RC SWs with CBs. Oh *et al*. [48] proposed and experimentally investigated an isolated hybrid device for CBs comprising HDR and a U-shaped steel damper. The results of the tests were compared with those of a conventional CB, showing how the hybrid device improved the seismic performance of the system and protected the shear wall from damage. Li *et al.* [49] experimentally investigated through quasi-static cyclic tests a hybrid RCB consisting of an I-shaped steel beam with multiple low-yield-point steel webs paralleled to each other and multiple layers of viscoelastic material bonded to multiple steel plates. The combined damper showed superior behavior during the cyclic loading tests and better performance during successive cyclic tests on a 1/2-scale coupled shear wall specimen incorporated with the replaceable damper[50]. The same device was recently investigated through extensive numerical simulations by the same Authors [51].

Although some pilot studies focused on such solutions, it is worth noticing that most of the experimental research focused on quasi-static tests [49,50] or was limited to the study of the isolated device [48], thus highlighting the need for advanced research investigating the dynamic response of the entire system. The present work experimentally investigates, through shaking table tests, the seismic performance of RC SW systems with RCBs equipped with hybrid dampers composed of a combination of metallic and HDR-based devices working in parallel. The seismic performance of the system is assessed by three sets of ground motion records scaled to represent a wide range of seismic intensities. The shaking table tests involved two 3D 7-story model structures, including one novel SWs with the proposed RCBs and, for comparison purposes, one SWs structure with conventional RC CBs (respectively named SW-RCBs and SW-CBs). The experimental results are successively used to develop and validate numerical models in OpenSees [52].

The paper is organized as follows: Section 2 describes the proposed hybrid RCB and its design procedure; Section 3 describes the case study structure and the specimens for the experimental tests; Section 4 describes the shaking table test program, the ground motion records, and the instrumentation; Section 5 describes the experimental results and compares the seismic performance obtained by using the conventional and innovative systems; while Section 6 describes the numerical modeling strategy of the two test specimens, compares the results obtained from the non-linear analyses and shaking table tests and perform a parametric study on the influence of some design parameters. The paper ends with key conclusions and recommendations for future research.

## 2. REPLACEABLE COUPLING BEAM (RCB) WITH HYBRID DEVICE

### *2.1 Concept*

Figure 1(A) shows the coupled RC SWs, while Figure 1(B) and (C) show, respectively, the RCBs and the details of the hybrid device. Figure 1(B) shows the non-replaceable parts of the RCB, which connect the hybrid device through end-plate bolted connections, thus allowing easy removal and replacement of the device after major earthquakes. The non-replaceable part is composed of RC beams with an embedded steel section with shear studs extending into the SW and welded to end-plate 2. The embedded steel section with studs evenly distributes the shear force transmitted from the end-plate onto the non-replaceable part. The hybrid device in Figure 1(C) comprises one metallic and two viscoelastic devices working in parallel. The metallic device has a welded I-shaped steel section made of low-yield-point steel, while the viscoelastic devices are made of two layers of HDR material bounded between three steel plates and connected to the steel end-plates through two steel blocks. These devices are arranged to work in parallel and are activated under shear deformations of the RCBs, as shown in Figure 1(D). This combination of metallic and viscoelastic devices can be optimized and allows calibrating both stiffness and energy dissipation capacity and provides better performances for a wide range of vibration intensities, including seismic (small- and large-intensity) and wind loads. As shown in Figure 1(E), during small-intensity earthquakes or high-intensity wind loads, the viscoelastic devices deform and generate damping forces through shearing of the HDR material, while the metallic device remains elastic and only provides stiffness to the system. Conversely, during high-intensity earthquakes, the metallic device yields to anticipate energy dissipation through plastic deformation. The ultimate response of the hybrid device can be obtained by superimposing the behavior of the metallic and viscoelastic devices, as shown in Figure 1(E).

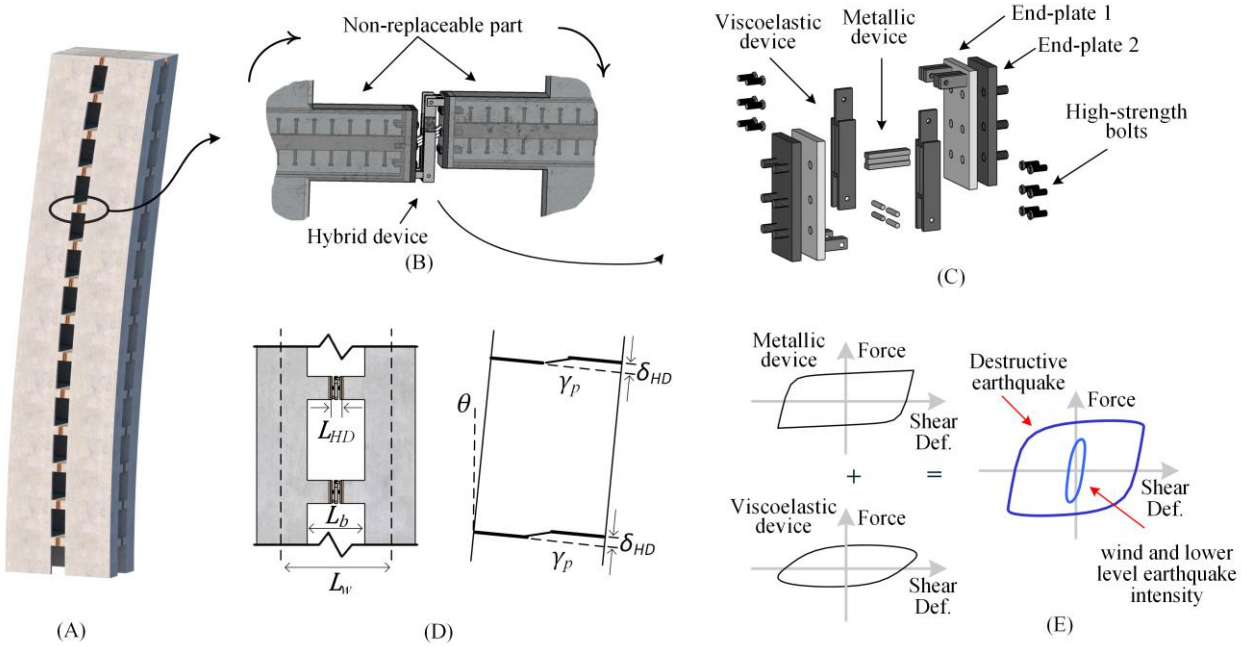


**FIGURE 1** Hybrid Replaceable Coupling Beam (RCB): (A) Coupled Shear Walls (SWs) with RCBs; (B) Hybrid device and non-replaceable part of the RCB; (C) Hybrid device; (D) Deformed shape of the SWs and shear behavior of the hybrid device; (E) Cyclic response of the hybrid device under different levels of input intensity.

### *2.2 Design procedure*

The design of the RCBs follows the design of a conventional RC SWs structure with CBs. The conventional SWs structure is designed to have a ductile failure mode by avoiding the formation of shear mechanisms, controlling the axial compressive force ratio in the SWs and incorporating boundary elements. The 'equivalent' conventional RC SWs with CBs is initially designed according to standard guidelines [2,53,54], allowing the definition of the required moment and shear

capacity of the CBs (*i.e.*, $M_{CB}$ and $V_{CB}$) and the expected peak drifts ratio $\theta_u$. Knowledge of these parameters represents the starting point for the design of the RCBs. Additionally, the design of the 'equivalent' conventional structure provides some indications for the definition of the drift ratio $\theta_y$ at which the metallic device yields and begins to dissipate energy. This value can be assumed to correspond to the drift ratio at which no damage would be expected (*e.g.*, drift corresponding to the intensity of 'frequent' earthquakes).

As previously mentioned, the response of the hybrid device is obtained by superimposing the behavior of the metallic and viscoelastic devices, and their combination could be optimized to meet the performance objectives for the different types/intensities of vibration loads. In the present study, the force developed by the hybrid device ($V_{HD}$) at the peak drifts ratio ($\theta_u$) is assumed equal to the force of the CB (*i.e.*, $V_{HD} = V_{CB}$) and is equally distributed between the metallic ($V_m$) and viscoelastic devices ($V_{ve}$), *i.e.*, the ratios $\psi = V_m/V_{HD}$ and $\chi = V_{ve}/V_{HD}$ are equal to 0.5. The optimization of the $\psi$ and $\chi$ ratios is beyond the scope of the present paper; however, the results of a numerical parametric study are presented in Section 6 to provide some preliminary insights on this matter.

According to the deformation mechanism shown in Figure 1(D), the drift ratio, the link rotation, and the shear displacement within the hybrid device are related to each other by the following relationships:

$$\gamma_p = \theta \times L_w/L_{HD} \qquad \delta_{HD} = \gamma_p \times L_{HD} \tag{1}$$

where $\theta$ is the drift ratio of the coupled SWs, $L_w$ is the distance between centroids of each SW, and $L_{HD}$ is the span of the hybrid device. Knowing the yielding and peak drifts ($\theta_y$ and $\theta_u$), these equations provide the yielding and peak rotations ($\gamma_{p,y}$ and $\gamma_{p,u}$) and displacements ($\delta_{HD,y}$ and $\delta_{HD,u}$).

Knowing the shear force in the metallic device (*i.e.*, $V_m = \psi V_{HD}$) at the peak link rotation ($\gamma_{p,u}$) and the rotation corresponding to the link yielding ($\gamma_{p,y}$), the design of the metallic device follows the procedure typically used for steel links in shear (*e.g.*, AISC 341-10 [55]) which allows to defines its key dimensions. Similarly, knowing the shear force in the viscoelastic device (*i.e.*, $V_{ve} = \chi V_{HD}$) at the peak displacement ($\delta_{HD,u}$), the design of the viscoelastic devices focuses on defining the number and dimensions of the layers of HDR material.

The non-replaceable parts of the RCBs are designed following the capacity design approach and, hence, to have sufficient overstrength to ensure they remain undamaged. The capacity design criteria are controlled by an overstrength factor $\xi$ which amplifies the required bending moment and shear capacity of the non-replaceable components of the RCBs (*i.e.*, $V_n \geq \xi V_{HD}$ and $M_n \geq \xi V_{HD} \times L_b/2$). Hence, the dimensions of the non-replaceable section of the RCBs are determined according to the following equations [2]:

$$M_n = f_y A_s h_0/\gamma_{RE} \geq \xi V_{hd} \times L_b/2 \tag{2}$$

$$V_n = 1.6 \times [0.6 f_{y,e} h_e t + (0.166\sqrt{f_c} b h_0 + f_{y,v} A_{sv} h_0/s)] \geq \xi V_{hd} \tag{3}$$

where $f_y$, $f_{y,v}$, $f_{y,e}$, and $f_c$ are, respectively, the yield strength of the longitudinal rebars, stirrups, embedded steel section, and concrete of the RCBs; $h$ and $b$ are, respectively, the height and width of the RCBs; $a_s$ is the thickness of the concrete cover and $h_0$ is the effective height (*i.e.*, $h_0 = h - 2a_s$) of the RCBs; $A_s$ and $A_{sv}$ are, respectively, the area of the longitudinal rebars and stirrups; $s$ is the stirrup spacing; $t_e$ and $h_e$ are respectively the width and high of the embedded steel section, while $\gamma_{RE}$ is the seismic resistance capacity factor, which is taken as 0.75 [53].

Moreover, to ensure that the RCBs are characterized by sufficient stiffness with respect to the conventional CBs and to guarantee the lateral stiffness of the coupled shear wall, the stiffness of the RCBs should not fall below that of traditional CBs after cracking. This requirement leads to the following inequality $K_{RCB}/K_{CB} \geq 0.7$ [56], where $K_{CB}$ corresponds to the stiffness of the conventional RC CBs, while $K_{RCB}$ corresponds to the stiffness of the RCBs accounting for the deformability contributions of the non-replaceable parts and the hybrid device. The stiffness $K_{CB}$ can be calculated as follows:

$$K_{CB} = \frac{1}{L_b{}^3/12E_cI + kL_b/G_cA} \tag{4}$$

where $E_c$ and $G_c$ are the Young's and shear modulus of the RC; $I$ and $A$ are the moment of inertia and area of the cross-section, while $k$ is the shape factor taken as 1.2 for rectangular cross-sections. The contribution of the floor slab to the CBs strength and stiffness was evaluated by considering a slab effecting width of $l/6$, where $l$ represents the span length. On the other hand, the stiffness $K_{RCB}$ can be calculated as follows:

$$K_{RCB} = \frac{1}{\Delta_{RCB}} = \frac{1}{\Delta_{n,M} + \Delta_{n,V} + \Delta_{HD,M} + \Delta_{HD,V} + \Delta_\theta} \tag{5}$$

where $\Delta_{RCB}$ is the displacement of the RCB in the vertical direction under a unit force and has several contributions: $\Delta_{n,M}$ and $\Delta_{n,V}$ are, respectively, the bending and shear displacement of the non-replaceable parts of the RCBs; $\Delta_{HD,M}$ and $\Delta_{HD,V}$ are, respectively, the bending and shear displacement of the hybrid device; and $\Delta_\theta$ is the vertical displacement due to the relative rotation of the non-replaceable and replaceable sections. These contributions can be calculated as follows:

$$\Delta_{n,M} = \frac{{L_n}^3}{12(E_{nc}I_{nc}+E_{ne}I_{ne})} \qquad \Delta_{n,V} = \frac{1.2L_n}{G_{nc}A_{nc}+G_{ne}A_{ne}} \tag{6a}$$

$$\Delta_{HD,M} = {L_{HD}}^3/12E_mI_m \qquad \Delta_{HD,V} = \frac{1}{\frac{G_mA_m}{kL_{HD}}+\frac{G_1nA_E}{t_E}} \tag{6b}$$

$$\Delta_\theta = \frac{L_{HD}{L_n}^2+2L_nL_{HD}{}^2}{8(E_{nc}I_{nc}+E_{ne}I_{ne})} \tag{6c}$$

where $L_n$ is the span of the non-replaceable section; $E_{nc}$, $G_{nc}$, $A_{nc}$, and $I_{nc}$, are, respectively, Young's modulus, shear modulus, area, and moment of inertia of the concrete section; $E_{ne}$, $G_{ne}$, $A_{ne}$, $I_{ne}$ are, respectively, Young's modulus, shear modulus, area, and moment of inertia of the embedded steel section; $E_m$ ,$G_m$, and $I_m$ are, respectively, Young's modulus, shear modulus, and moment of inertia of the steel link.

Other non-dissipative and rigid components of the RCBs, such as the connections, end-plates, etc., are designed according to capacity design rules, ensuring adequate overstrength.

## 3. CASE STUDY STRUCTURES

### *3.1 Prototype structure and coupled shear wall specimens*

Figure 2(A) shows the plan view of the prototype building selected for case study purposes. It consists of a 7-story office building with RC columns and beams providing mainly resistance to the gravity load and two SWs with CBs providing resistance to the horizontal loads. It has constant interstory heights of 3.60 m and a plan layout of six and three bays, in *x*- and *y*-direction, with constant spans of 5.2 and 7.2 m, respectively. In addition to the self-weight of the structural components and slabs, the permanent design load is assumed equal to 2 kN/m$^2$, while the live load at each story is assumed equal to 4 kN/m$^2$, giving a total mass of the structure for the seismic design combination of 499.359 tons. The seismic design is performed according to the Chinese seismic design code (GB 50011-2010) [2] considering a seismic fortification intensity of 8 with a design PGA equal to 0.20g for 'moderate' earthquakes (*i.e.*, probability of exceedance of 10% in 50 years) and 0.07g. for 'frequent' earthquakes (*i.e.*, probability of exceedance of 63% in 50 years). The building is assumed to be Type C and the soil type to be Class III (*i.e.*, soft soil).

The present study focuses on the experimental assessment of the coupled SWs system. The coupled SWs system was extracted from the prototype structure [see Figure 2(A)], and a 1/4 scaled model was used for the experimental tests according to the shaking table capabilities. The model was designed according to the length, stress, and acceleration similitude law ($S_l$, $S_\sigma$, and $S_a$). Table 1 reports the comprehensive list of similitude scaling factors between the prototype and the specimens.

**TABLE 1** Similitude scaling factors from the prototype to the specimens.

| Variable | Equation | Scaling factor | Notes |
|---|---|---|---|
| Length | $S_l$ | 0.25 | Controlling factor |
| Young's modulus | $S_E$=$S_\sigma$ | 1.0 | |
| Stress | $S_\sigma$ | 1.0 | Controlling factor |
| Strain | $S_\sigma$/$S_E$ | 1.0 | |
| Density | $S_\sigma$/($S_a$×$S_l$) | 2.0 | |
| Force | $S_\sigma$×$S_l^2$ | 0.04 | |
| Mass | ($S_\sigma$×$S_l^2$)/$S_a$ | 0.031 | |
| Frequency | $S_l^{-0.5}$×$S_a^{0.5}$ | 2.828 | |
| Time | ($S_l$×$S_a$)$^{0.5}$/$S_a$ | 0.354 | |
| Velocity | ($S_l$×$S_a$)$^{0.5}$ | 0.707 | |
| Acceleration | $S_a$ | 2.0 | Controlling factor |

Two specimens were built considering coupled SWs systems, respectively, with conventional RC CBs (SW-CBs) and with the proposed RCBs (SW-RCBs). Except for the coupling beams, the geometry, configuration, materials, and reinforcements of the SWs were the same for both specimens. The specimens had plan dimensions of 1.3 m × 1.8 m, a total height of 6.3 m, and interstory heights of 0.9 m [see Figure 2(B) and (H)]. The thickness of the shear wall and the floor slab were 75 mm and 40 mm, respectively. It is worth mentioning that the coupling beams have slightly different dimensions in *x*- and *y*-directions. According to the scaling factors in Table 1, the mass of each model should have been equal to 15.480 tons. However, being unable to scale the density of the materials, the total mass of the model amounted

to 6.524 tons. Therefore, additional mass blocks with a total weight of 8.956 tons were uniformly distributed on the slabs at different stories of the specimens. To prevent any interference with the CBs, the additional masses were evenly distributed in two layers across the floor and positioned to avoid the areas directly above the beams. The dimensions and reinforcement details (placement, amount, and dimension of the stirrups, distribution, and longitudinal rebars) of the main components of the specimens were derived from the prototype structure based on the similitude law and shown in Figure 2(C) to (G). Figure 2(C) refers to the non-replaceable beam segments of the RCBs, while Figure 2(D) refers to the CBs used in the conventional system. Figure 2(C) also shows the embedded steel section and the studs in the non-replaceable parts of the RCBs. The embedded steel section was 20 mm × 40 mm with D6 (*i.e.*, diameter = 6 mm) shear studs with a height of 40 mm. All the other section details are for components common to both specimens.

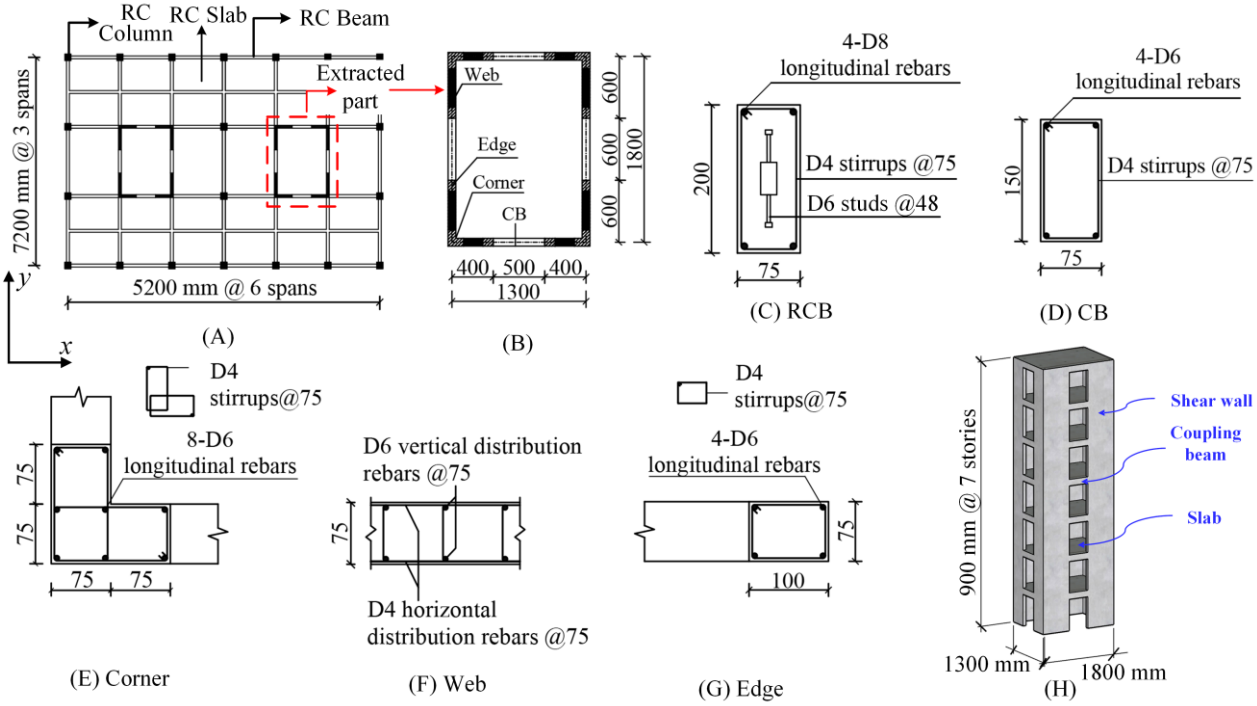


**FIGURE 2** (A) Plan view of the prototype case study building; (B) Plan view of the coupled shear walls specimens; (C) to (G) Cross-sections and reinforcement details of the non-replaceable beam segment of the Replaceable Coupling Beams (RCBs), of the Coupling Beams (CBs), of the Corners, Webs and Edges; (H) Elevation view. [units in mm].

### *3.2 Material properties*

Both specimens were constructed simultaneously with a conventional cast-in-place method, with concrete poured and cured onsite one story at a time. The design strength of the concrete was C30 (*i.e.*, cubic compressive strength $f_{cu}$ = 30 MPa). Six concrete samples (*i.e.*, three cubes and three rectangular prisms) were cast for each story from both specimens to characterize the material. These samples were tested simultaneously at the beginning of the shaking table sequence, hence informing on the actual material properties of the tested specimens. Table 2 summarizes the average compressive strength ($f_{cu}$) and elastic modulus ($E_c$) of the material at the different stories, also including the curing days of the samples. It is noteworthy that the measured strength is lower than the design value in almost all cases and with a non-negligible variability among the different stories. However, this variation did not significantly affect the results, as successively discussed in Section 5. The strength grade of stirrups and distribution steel rebars was HPB300 (*i.e.*, $f_y$ = 300 MPa), while for longitudinal rebars was HRB400 (*i.e.*, $f_y$ = 400 MPa). Three coupons were tested for each type of steel rebar to evaluate the yield ($f_y$), ultimate ($f_u$) strength, elastic modulus ($E_s$) and average elongation at rupture ($\varepsilon_f$)of the materials. Table 3 summarizes the properties of the steel rebars used for the specimens. The steel material used for the embedded steel section was Q345 (*i.e.*, $f_y$ = 345 MPa).

**TABLE 2** Mechanical properties of the concrete.

| Property | Unit | Story 1 | Story 2 | Story 3 | Story 4 | Story 5 | Story 6 | Story 7 |
|---|---|---|---|---|---|---|---|---|
| $f_{cu}$ | MPa | 19.9 | 32.3 | 24.2 | 16.1 | 25.0 | 12.7 | 21.0 |
| $E_c$ | GPa | 22.3 | 31.4 | 29.5 | 20.0 | 25.0 | 20.6 | 26.9 |
| Curing days | days | 79 | 69 | 60 | 52 | 43 | 37 | 27 |

**TABLE 3** Mechanical properties of the steel rebars.

| Property | Unit | D4 dist. & stirrups | D6 dist. | D6 long. | D8 long. |
|---|---|---|---|---|---|
| $f_y$ | MPa | 458 | 438 | 507 | 515 |
| $f_u$ | MPa | 539 | 464 | 582 | 607 |
| $E_s$ | GPa | 159 | 159 | 183 | 190 |
| $\varepsilon_f$ | % | 18.3 | 20.8 | 24.7 | 25.5 |

### *3.3 Hybrid Device*

Figure 3 shows the details of the hybrid device used in the *x*-direction. The hybrid devices have slightly different dimensions in the *x*- and *y*-directions, with spans respectively equal to 70 mm and 75 mm. Each viscoelastic device consists of two layers of HDR material (with stiffness and loss factor respectively equal to 560 kN/m and 0.5) with dimensions of 30 mm × 80 mm × 5 mm, bonded between three steel plates [see Figure 3(B)] and providing a maximum design force of 4.5 kN. The metallic device is composed of a welded I-shaped beam section. The height and width of the flanges are 8 mm × 15 mm and are the same for the *x*- and *y*-directions. Conversely, the height and width of the web are slightly different and equal to 10 mm × 8 mm in the *x*-direction and 12 mm × 8 mm in the *y*-direction [see Figure 3(B)]. The two ends of the I-shaped metallic device are welded to the end-plates. The steel material used for the end-plates and all the components of the viscoelastic device has a yield strength of 345 MPa. Conversely, the metallic devices use a low-yield-point steel BLY100 with a yield strength of 173 MPa (obtained as an average of three coupon tests of the material).

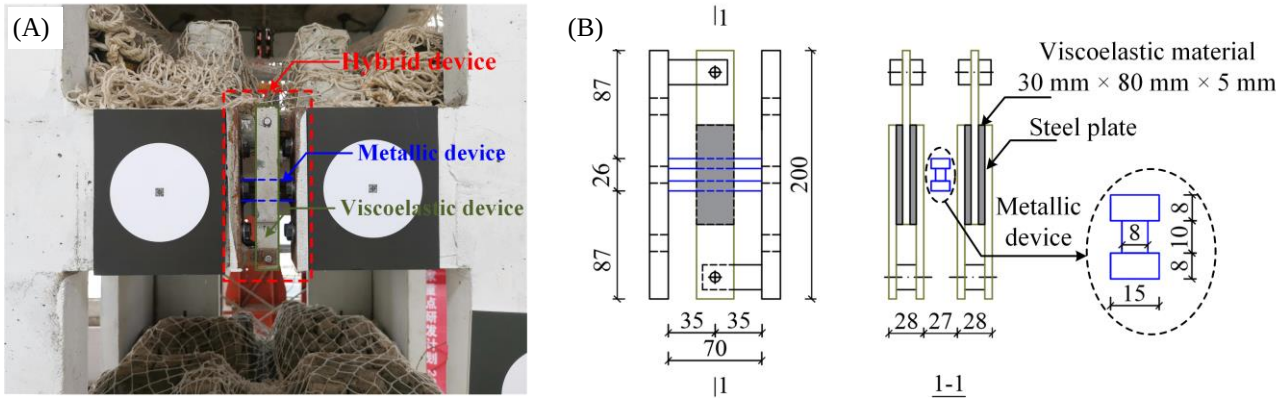


**FIGURE 3** Details of the hybrid device of the specimen in the *x*-direction. [units in mm].

## 4. TEST PROGRAM

### *4.1 Test setup and test matrix*

Figure 4 shows the two model structures settled on the shaking table. The shaking table tests were conducted in the State Key Laboratory of Disaster Reduction in Civil Engineering at Tongji University.

Three pairs (*i.e.*, *x*- and *y*-components) of ground motion records were selected for the shaking table tests, including two natural records and one artificial earthquake. These include: *1)* Shanghai – the one-directional artificial seismic record selected from the appendix of Shanghai Code for seismic design of buildings [57]; *2)* El Centro – the 1940 Imperial Valley earthquake recorded at El Centro station, California; and *3)* Northridge – the 1994 Northridge earthquake recorded at the Sylmar Olive View FF in Sylmar, California. The vertical component of the ground motion records was neglected.

Figure 5(A)~(E) shows the ground motion records selected for the tests. The acceleration response history of the input excitations used during the shaking table tests was successively scaled in time with a coefficient of 0.354 to satisfy the scaling identity requirements. Each natural earthquake record has two horizontal orthogonal components, denoted as h1 and h2. Conversely, the Shanghai artificial record only has one horizontal component. Figure 5(F) shows the acceleration response spectra of the records together with the design spectrum defined according to the Chinese seismic design code for buildings (GB 50011–2010) [2]. The records are scaled to match the PGA of the prototype structure for 'frequent' earthquakes (*i.e.*, PGA = 0.07g). The comparison shows a good agreement between the design seismic input and the selected records.

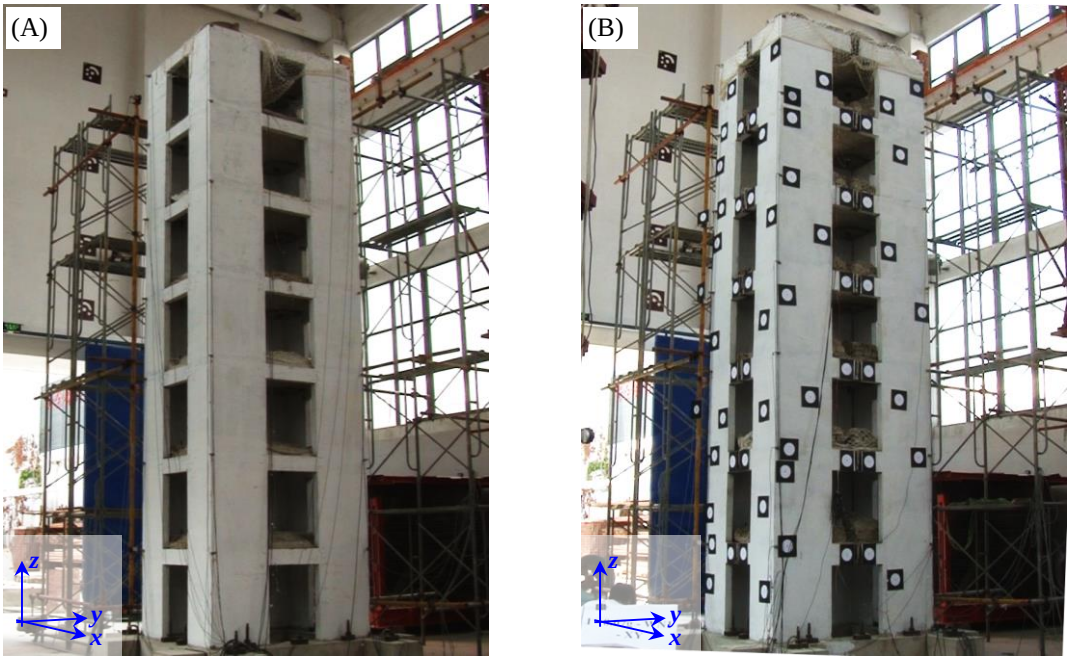


**FIGURE 4** Structure models installed on the shaking table: (A) SW-CBs; and (B) SW-RCBs.

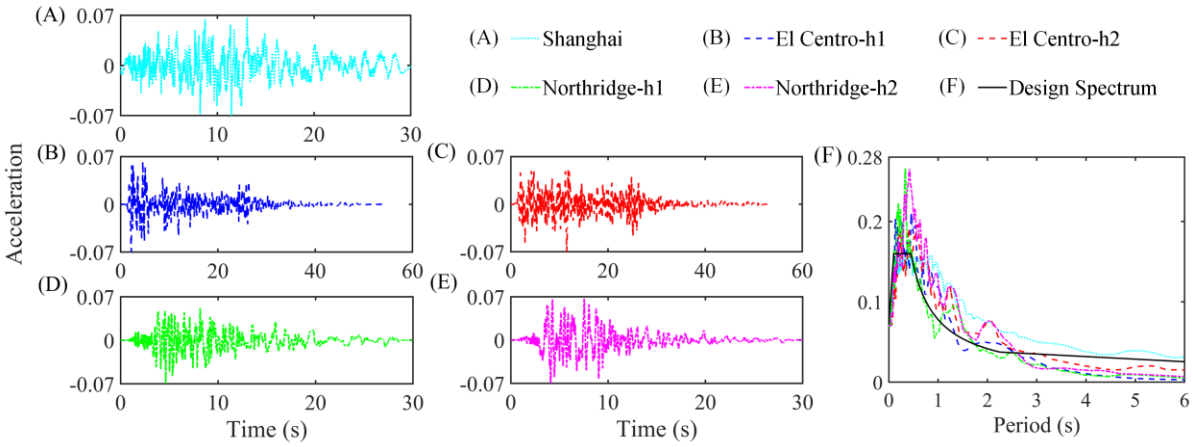


**FIGURE 5** Acceleration response history of the selected ground motions records and comparison with the design spectrum.

Table 4 summarizes the test matrix used during the shaking table tests. The input motions were divided into four intensity levels with gradually increasing PGA equal to 0.14g, 0.40g, 0.60g, and 0.80g. It is worth reminding the reader that the scaling factor for the acceleration is equal to 2.0 (see Table 1), and hence, the 0.14g intensity in the shaking table test represents the 'frequent' earthquake intensity of the prototype (*i.e.*, PGA = 0.07g). Similarly, the 0.40g intensity in the shaking table test represents the 'moderate' earthquake intensity in the prototype (*i.e.*, PGA = 0.20g). Higher intensities have been used to assess the performance of the system at collapse. During the shaking table tests, the duration of each selected seismic excitation shown in Figure 5 was compressed according to the time scaling factor of 0.354 (see Table 1). Before and after each intensity level, bi-directional white noise excitation tests were conducted to monitor the changes in the specimens' dynamic properties. The three ground motions (*i.e.*, Shanghai, El Centro, and Northridge) were simulated for each seismic intensity. For the Shanghai record, the one-directional excitation was applied independently in the *x*- and *y*-directions (*e.g.*, Tests 2 and 3 in Table 4). Conversely, for the El Centro and Northridge ground motions, multi-directional excitations were applied in the *x*- and *y*-direction, considering the two components h1 and h2 simultaneously. The PGAs of the h1 and h2 components were scaled to have a ratio of 1:0.85 (*i.e.*, h1 was assumed to be the main acceleration component). The h1 component was applied alternatively in the *x*- and *y*-directions, simultaneously with the h2 component in the other direction (*e.g.*, Tests 4 and 5 in Table 4 corresponds to the El Centro record with a PGA = 0.14g – In Test 4 the h1 component is applied in the *x*-direction and 0.85% of the PGA of the h2 component is simultaneously applied in the *y*-direction – In Test 5 the h1 component is applied in the *y*-direction and 0.85% of the PGA of the h2 component is simultaneously applied in the *x*-direction). Additional tests were successively conducted only on the SW-RCBs specimen under the three ground motions for higher intensities with PGAs = 1.04g, 1.24g, and 1.40g.

**TABLE 4** Test matrix.

| Test | PGA ( g ) | Record | Input PGA ( g ) | |
|---|---|---|---|---|
| | | | *x*-dir | *y*-dir |
| 1 | | White noise | 0.07 | 0.07 |
| 2 | 0.14 | Shanghai | PGA | - |
| 3 | | Shanghai | - | PGA |
| 4 | | El Centro | PGA | 0.85PGA |
| 5 | | El Centro | 0.85PGA | PGA |
| 6 | | Northridge | PGA | 0.85PGA |
| 7 | | Northridge | 0.85PGA | PGA |
| 8 | | White noise | 0.07 | 0.07 |
| 9 | 0.40 | Shanghai | PGA | - |
| 10 | | Shanghai | - | PGA |
| 11 | | El Centro | PGA | 0.85PGA |
| 12 | | El Centro | 0.85PGA | PGA |
| 13 | | Northridge | PGA | 0.85PGA |
| 14 | | Northridge | 0.85PGA | PGA |
| 15 | | White noise | 0.07 | 0.07 |
| 16 | 0.60 | Shanghai | PGA | - |
| 17 | | Shanghai | - | PGA |
| 18 | | El Centro | PGA | 0.85PGA |
| 19 | | El Centro | 0.85PGA | PGA |
| 20 | | Northridge | PGA | 0.85PGA |
| 21 | | Northridge | 0.85PGA | PGA |
| 22 | | White noise | 0.07 | 0.07 |
| 23 | 0.80 | Shanghai | PGA | - |
| 24 | | Shanghai | - | PGA |
| 25 | | El Centro | PGA | 0.85PGA |
| 26 | | El Centro | 0.85PGA | PGA |
| 27 | | Northridge | PGA | 0.85PGA |
| 28 | | Northridge | 0.85PGA | PGA |
| 29 | | White noise | 0.07 | 0.07 |

### *4.2 Instrumentation*

A total of 34 accelerometers and 14 pull-wire type displacement sensors were installed on each model to measure the acceleration and displacement responses. Figure 6(A) shows the locations of the accelerometers installed on the specimens. Horizontal accelerometers were installed on the seven stories and the base connection with the shaking table. One corner of the specimen was equipped with accelerometers in both directions while the other two corners were equipped with accelerometers independently in *x*- and *y*-direction. Additionally, two vertical accelerometers were installed on the base connection with the shaking table to measure the response in the *z*-direction. Figure 6(B) shows the location of the 14 displacement transducers installed on the specimens. These were installed on the base connection, the first, third, fourth, fifth, and the top story to measure the displacements. Moreover, strain gauges have been strategically placed at steel rebars of the CBs and RCBs to monitor their local response on each floor, as shown in Figure 6(C). Additionally, the displacements of the specimen SW-RCB were monitored by a high-speed photogrammetric system controlling the reference points illustrated in Figure 4(B). This system also allowed measuring the displacements/deformations of the hybrid devices.

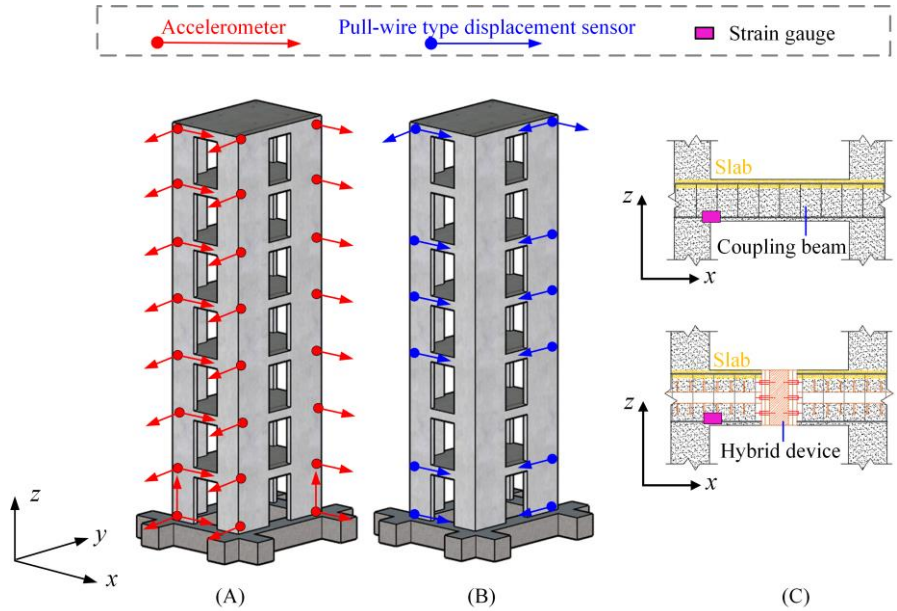


**FIGURE 6** Instrumentation: (A) Accelerometers; (B) Displacement transducers; (C) Strain gauges.

## 5. TEST RESULTS AND CRITICAL DISCUSSION

### *5.1 Dynamic properties and damage evolution*

The specimens were subjected to white noise tests before and after each seismic intensity to capture the evolution of the natural frequencies and vibration modes. Figure 7 shows the initial transfer functions (*i.e.*, Test 1 in Table 4) of both specimens in the *x*- and *y*-directions highlighting the first five vibration frequencies. The initial fundamental frequencies in the *x*- and *y*-direction are respectively 4.63 Hz and 6.00 Hz for specimen SW-CBs, and 4.5 Hz and 5.25 Hz for specimen

SW-RCBs. The lower frequencies of SW-RCBs (*i.e.*, 2.81% and 12.5% in *x*- and *y*-direction) are related to the slightly lower stiffness of the RCBs due to the discontinuity created by the hybrid device at the center.

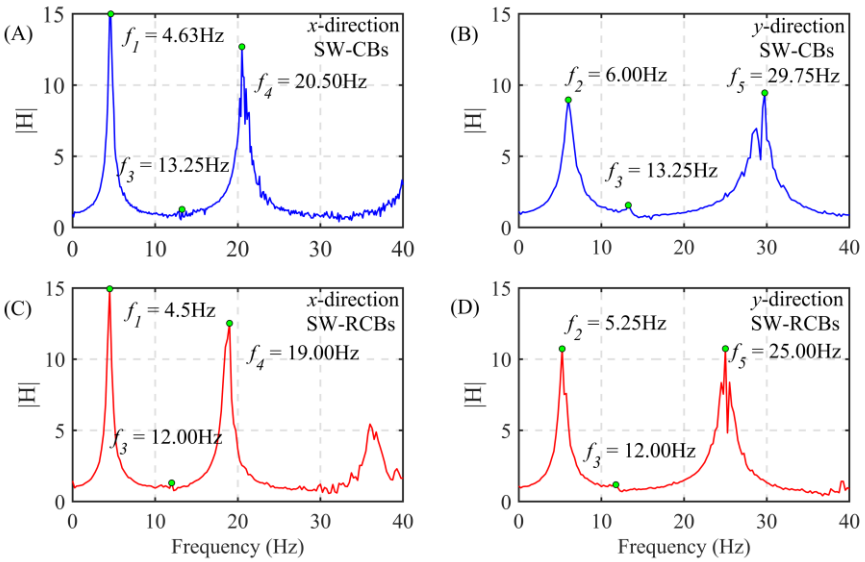


**FIGURE 7** Transfer functions from the initial white noise excitation - Test 1. SW-CBs specimen in (A) *x*- and (B) *y*-direction. SW-RCBs specimen in (C) *x*- and (D) *y*-direction.

The transfer functions in Figure 7 show small peaks between $f_1$ and $f_4$ for the *x*-, and between $f_2$ and $f_5$ for the *y*-direction. It could be anticipated that these interior peaks represent the torsional modes. The first three vibration modes of both specimens are in the following order: *1)* translation in *x*, *2)* translation in *y*, and *3)* torsion. The amplitude of the transfer functions of the torsional modes is relatively small [*e.g.*, 1.272 in Figure 7(A)], indicating that the vibration is dominated by translation. This is due to the regular layout and uniform distribution of mass and stiffness.

Figure 8 shows the evolution of the frequencies $f_1$, $f_2$, and $f_3$ measured before and after each seismic intensity level (*i.e.*, PGA equal to 0.14g, 0.40g, 0.60g and 0.80g – Tests 1, 8, 15, 22, 29 in Table 4) hence informing on the stiffness degradation as a consequence of the damage experienced in the structures. Figure 9 provides a similar comparison by showing the frequency degradation, defined as the ratio between the frequency reduction and the initial frequency. It can be observed that the specimen SW-CBs is subjected to a larger stiffness degradation, mostly experienced after the tests with small seismic intensities (*i.e.*, 0.14g and 0.40g). This is related to the higher damage experienced in the CBs with respect to the RCBs, as expected.

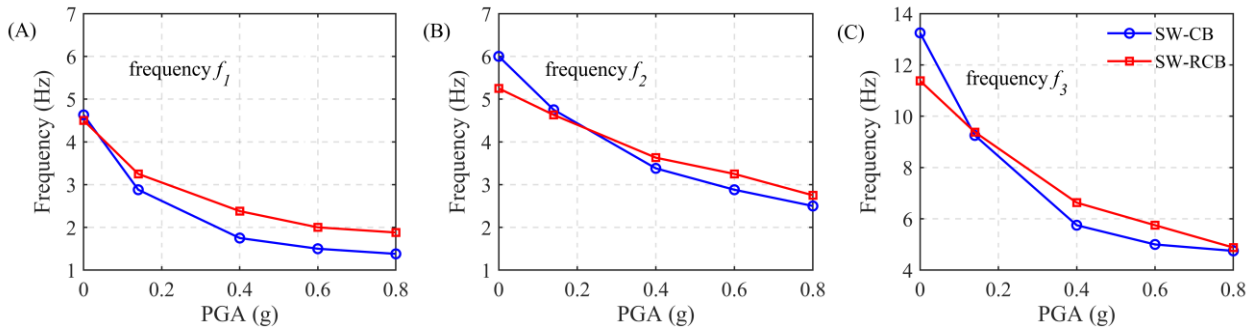


**FIGURE 8** (A) $f_1$; (B) $f_2$; and (C) $f_3$ frequency evolution after each seismic intensity level.

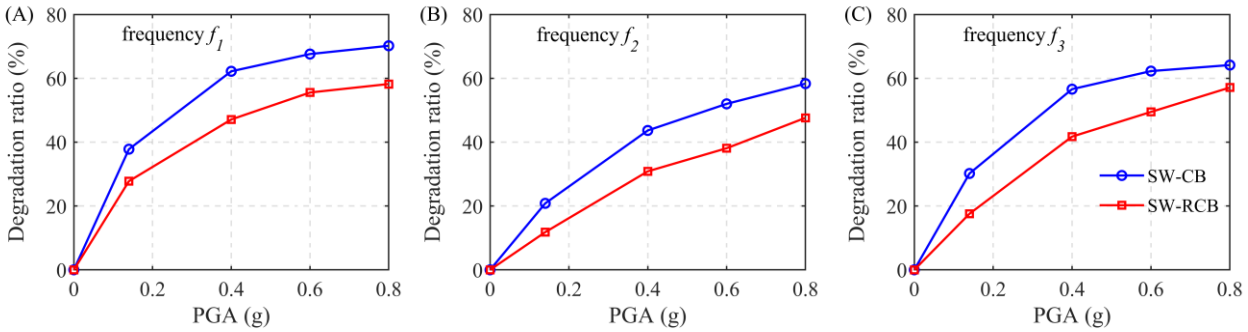


**FIGURE 9** (A) $f_1$; (B) $f_2$; and (C) $f_3$ frequency degradation after each seismic intensity level.

Figure 10 shows and compares the damage evolution at the end of the CBs and RCBs of the third story for both specimens. CBs and RCBs at other stories experience a similar response and are not reported here for the sake of brevity. Figure 10(A) and (E) show the damage condition after tests with PGA = 0.14g. Small visible cracks were observed in both specimens at the intersection between the coupling beams and the shear wall. More minor and fewer cracks were observed in the SW-RCBs compared to the SW-CBs. For the higher seismic intensity with PGA = 0.40g, the previous cracks further developed in width and propagated within the CBs of SW-CBs [Figure 10(B)]. Conversely, for the SW-RCBs, the previous cracks only slightly developed in length [Figure 10(F)]. Under this seismic intensity, it was already possible to observe some non-negligible shear deformation in the hybrid device. For PGA = 0.60g, the previously observed cracks within the CBs of SW-CBs became significantly larger, several diagonal cracks were detected within the SW, and there were signs of crushing of the concrete cover. Additional cracks were also observed in the shear wall [Figure 10(C)]. Conversely, the SW-RCBs only experienced a further extension of the previous cracks at the connection with the SWs and the cracks were not yet penetrated. No cracks were detected within the RCBs [Figure 10(G)], and the shear deformation in the hybrid devices was significantly increased. A vertical crack was observed in the shear wall. After the tests with the highest seismic intensity (PGA = 0.80g), the CBs underwent severe damage and plastic hinge rotation. The stirrups at the end of the CBs of the SW-CBs were partially exposed, the concrete cover was damaged, and concrete spalling was observed within the connection between the beam and the SWs. This damage pattern caused a significant reduction in the lateral stiffness of the structure [Figure 10(D)]. Conversely, crack in SW-RCBs were still limited and did not propagate within the RCB [Figure 10(H)]. As can be compared in Figure 10(D) and Figure 10(H), the crack generated in the SW-RCBs was delayed and exhibited limited propagation.

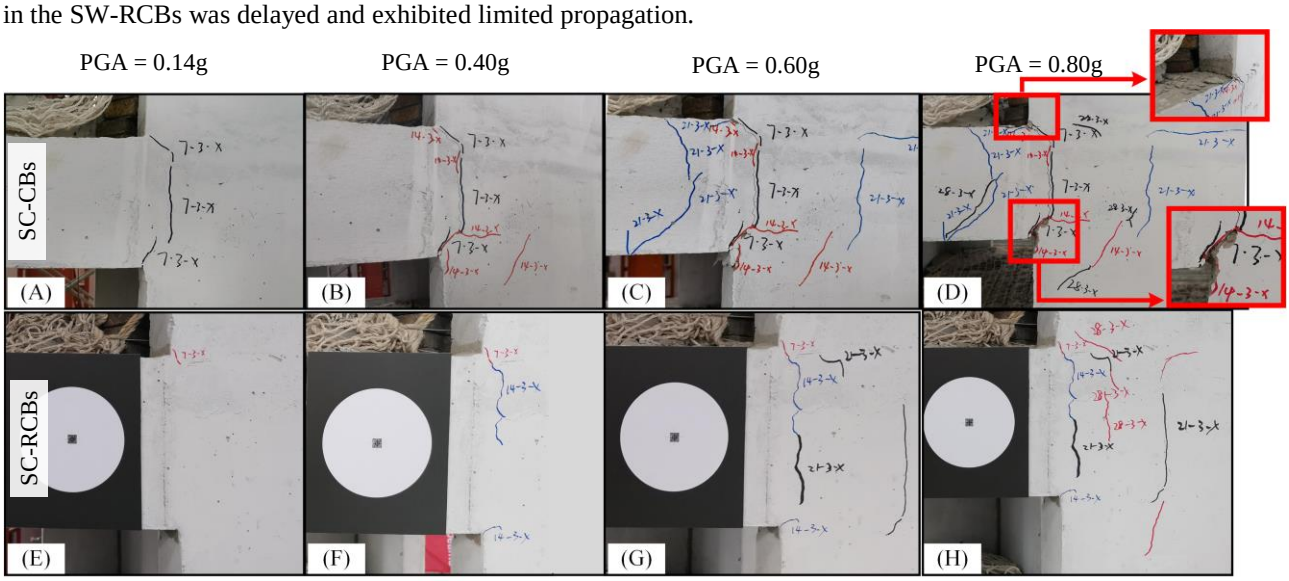


**FIGURE 10** Damage evolution at the end of CBs/RCBs of the third story after each seismic intensity level (*i.e.*, PGA equal to 0.14g, 0.40g, 0.60g, and 0.80g). (A) to (D) SW-CBs and (E) to (H) SW-RCBs.

Figure 11 shows the evolution of the damping ratio of the SW-CBs and SW-RCBs, considering the first three vibration modes. The damping ratios were similar at the beginning of the tests, and their difference gradually increased during the test due to the different levels of damage experienced. In particular, the SW-RCBs showed a lower damping ratio throughout the tests due to the lower damage experienced in the RCBs. Conversely, the SW-CBs specimen was subjected to cracks in the SWs and within the CBs, significantly contributing to the damping increase. It is worth highlighting that, in line with the results related to the stiffness degradation [Figure 8 and Figure 9], a significant damping increase was observed after the tests with small seismic intensities (*i.e.*, 0.14g and 0.40g). During the tests with PGA = 0.80g, the SW-CBs showed plastic hinges at several stories resulting in a significant increase in the damping ratio.

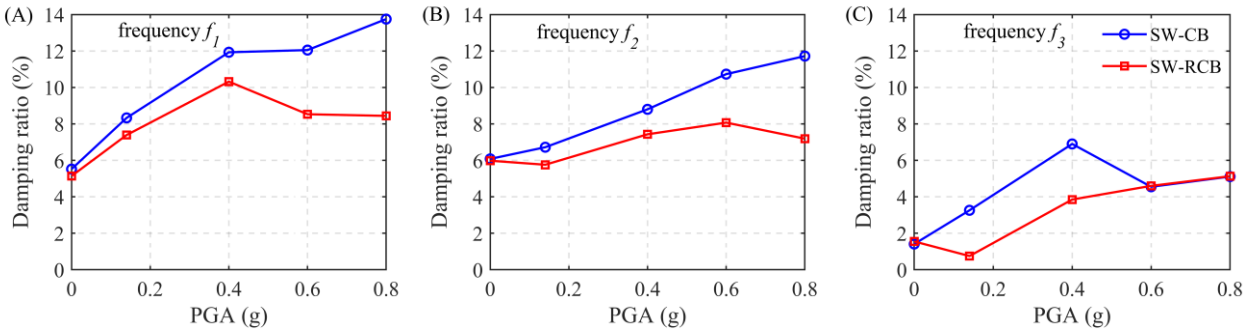


**FIGURE 11** Damping ratio of the first three vibration modes.

*5.2 Displacement response*

Figure 12 compares the top story displacement response histories of both specimens subjected to the three seismic excitations and for each seismic intensity level. It can be observed that the displacement response is more pronounced in the *x*- rather than the *y*-direction due to the geometry layout of the prototype structure. The SW-RCBs is subjected to lower displacements than the SW-CBs for all tests and intensities (*e.g.*, 37.3% lower for the 0.8g El Centro in *x*-direction, 24.9% lower for the 0.8g Shanghai in *x*-direction, 16.8% lower for the 0.6g Shanghai in *x*-direction, and 32.69% lower for the 0.6g Northridge in *y*-direction). The only exception is for the displacement in the *y*-direction for the tests with PGA = 0.14g [Figure 12(B)]. This was due to the larger deformability (*i.e.*, lower vibration frequency) in the *y*-direction of the undamaged SW-RCBs compared to the SW-CBs. However, the situation is immediately inverted for the following higher intensity (*i.e.*, PGA = 0.40g) due to the damage experienced by the SW-CBs and due to the higher dissipation capacity of the hybrid device for this intensity. In general, it can be observed that more significant differences exist for larger seismic intensities, and, among others, this is due to the damage evolution, which is more pronounced in the SW-CBs. Figure 12(A) and (B) also show that, although there is little difference at the initial stage of each seismic test run, the vibrations of the SW-RCBs are quickly dissipated and go to zero in a shorter time, thanks to the energy dissipation capacity of the hybrid device, especially for larger PGAs where also the metallic device is activated. This effect is more pronounced in the *x*-direction.

Figure 13 compares the peak interstory drifts (IDRs) along with the height of both specimens for the *x*- and *y*-direction and for the three considered ground motions. For small seismic intensities (*i.e.*, 0.14g and 0.40g), the IDRs distributions of the two models were similar in the *x*-direction, while some difference could be observed in the *y*-direction. For higher seismic intensities (*i.e.*, 0.60g and 0.80g), some differences can be observed in terms of amplitude and shape of the IDRs response between the two specimens. In addition to the larger drifts, the plot shows a less uniform distribution of the IDRs in the SW-CBs with large peaks at the third story in the *x*-direction due to the damage evolution of the CBs. Additionally, it is possible to notice that there are no significant differences in IDRs of SW-RCBs among the different seismic inputs.

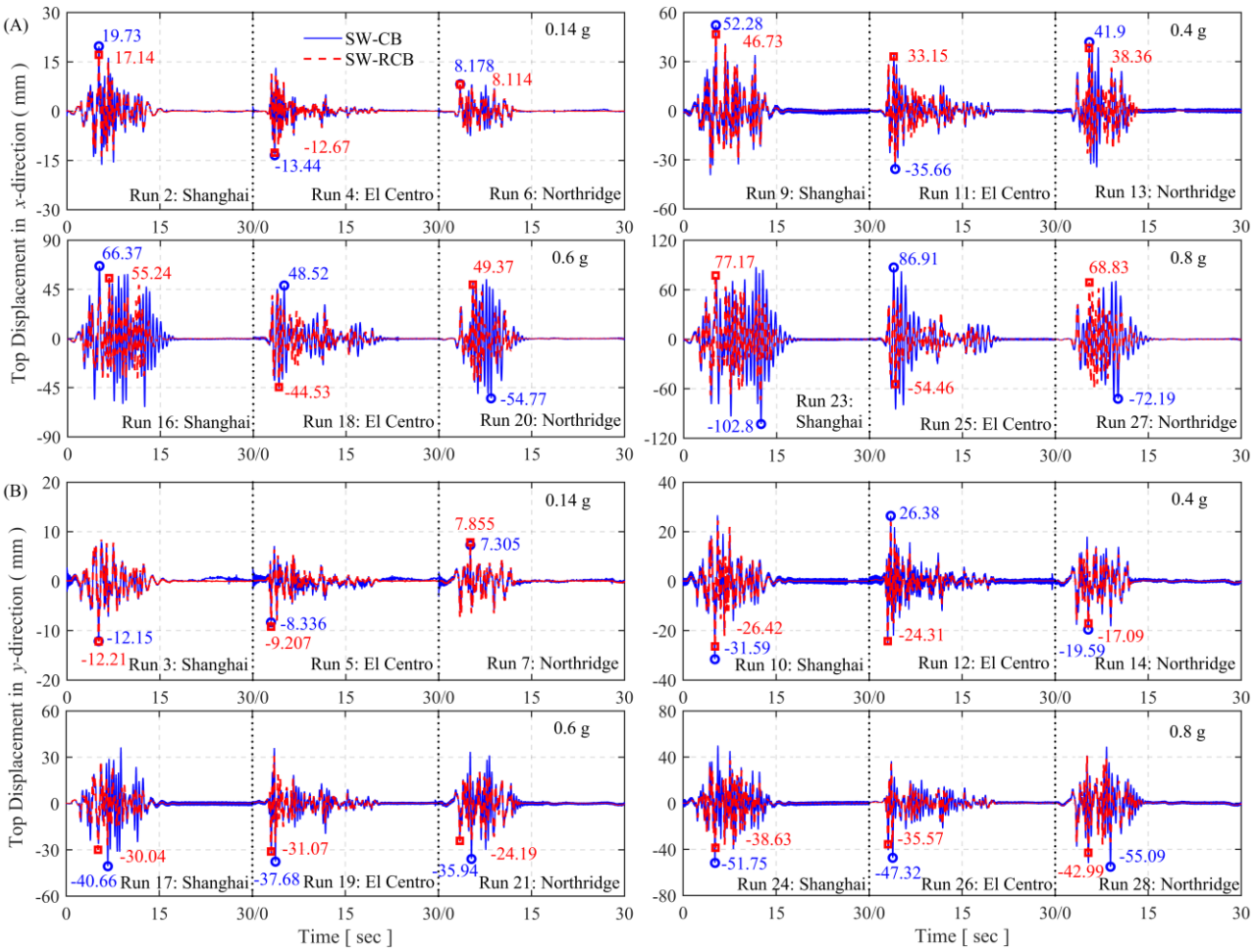


**FIGURE 12** Top story displacement response histories of the SW-CBs and SW-RCBs for the three seismic excitations and each seismic intensity level: (A) *x*- and (B) *y*-direction.

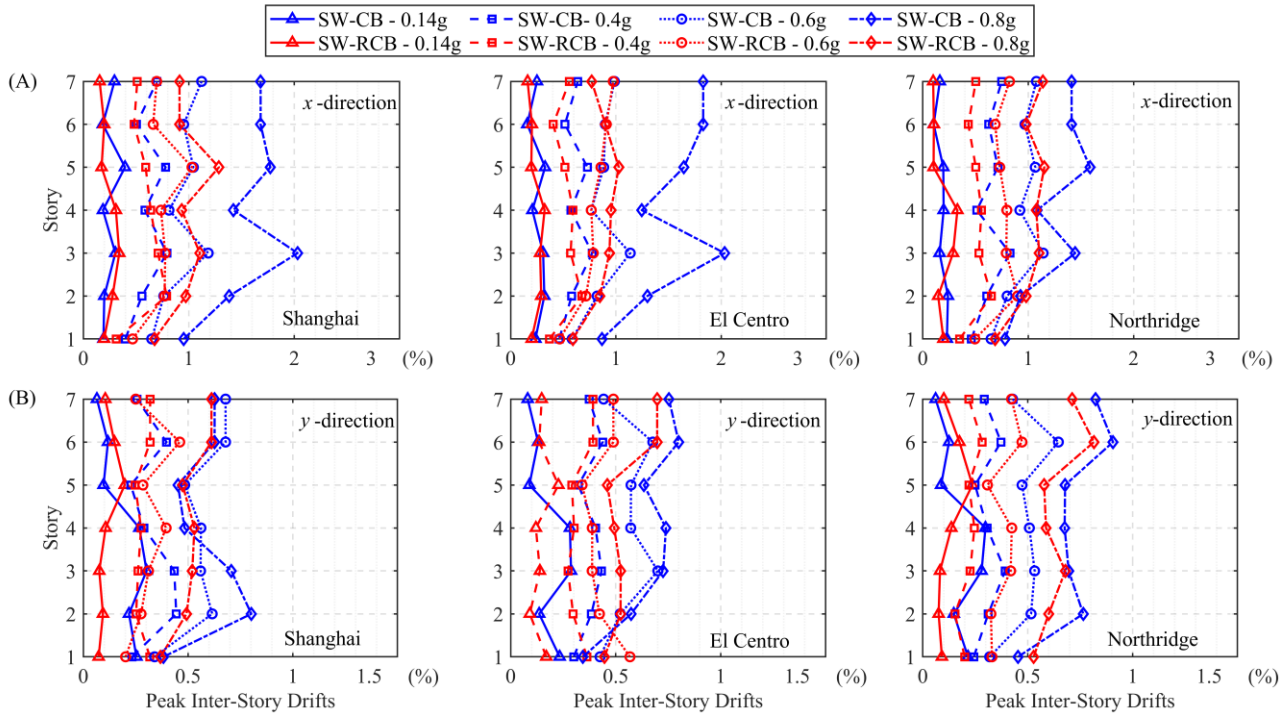


**FIGURE 13** Peak interstory drifts (IDRs) along with the height of the SW-CBs and SW-RCBs for the three seismic excitations and each seismic intensity level: (A) *x*- and (B) *y*-direction.

*5.3 Acceleration response*

Figure 14 compares the top story acceleration response histories of both specimens subjected to the three seismic excitations and for each seismic intensity level. The response histories of both specimens almost coincided at the initial stage of each test and began to deviate at a later stage. It is noteworthy that the SW-CBs exhibit larger acceleration responses in almost all cases, especially under the Northridge earthquake, demonstrating the benefits produced by the hybrid devices on the acceleration response. The reduction of the accelerations observed for the small-intensity earthquakes (*i.e.*, 0.14g) highlights the beneficial effects produced by the viscoelastic devices.

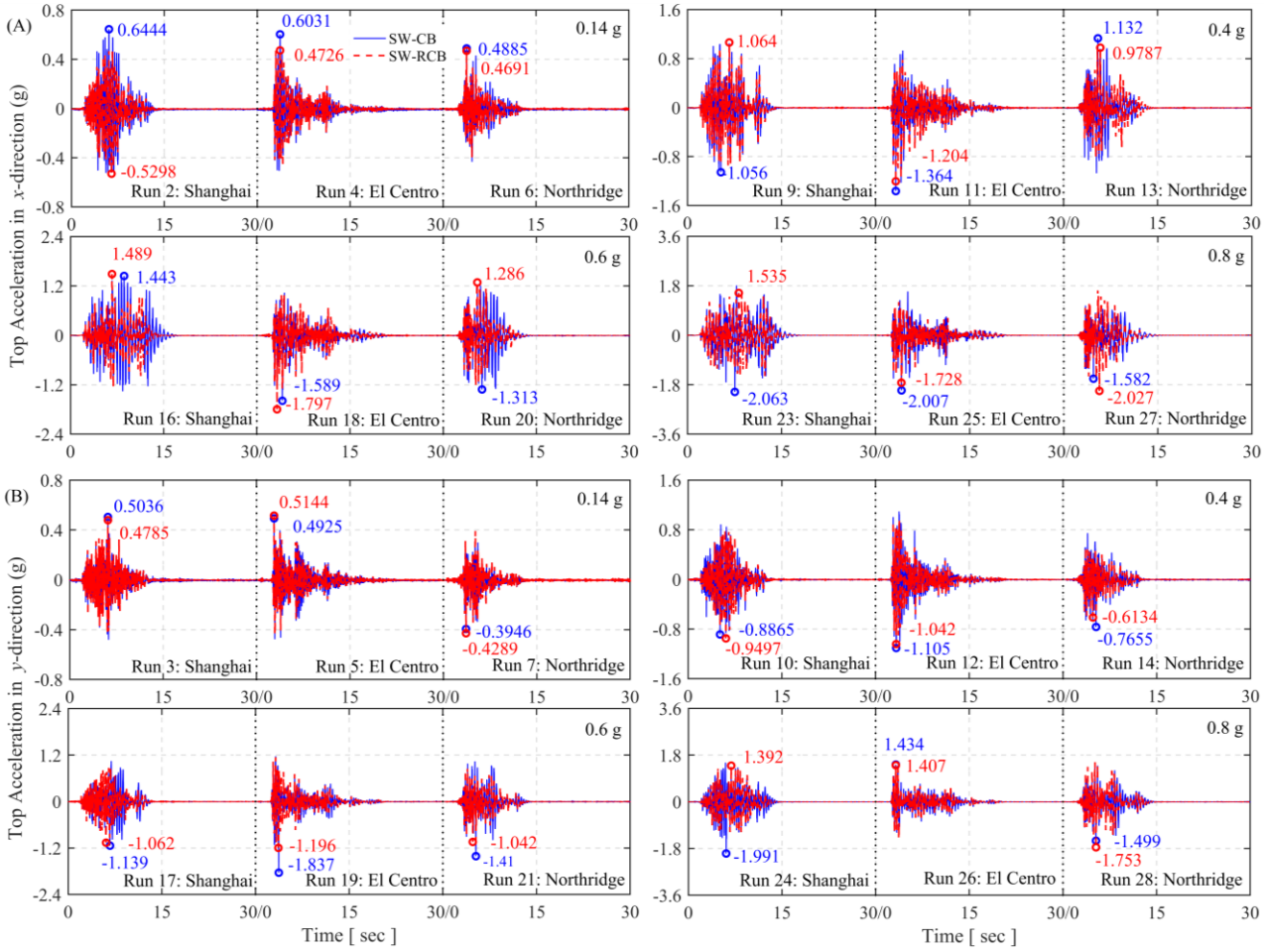


**FIGURE 14** Top story accelerations response histories of the SW-CBs and SW-RCBs for the three seismic excitations and each seismic intensity level: (A) *x*- and (B) *y*-direction.

Figure 15 compares the peak accelerations along with the height of both specimens for the *x*- and *y*-direction. The peak acceleration of the two specimens exhibited similar amplitude and distribution for PGAs of the seismic inputs up to 0.60g. The response difference between the two specimens tends to increase with the increase of seismic PGA. Obvious differences appeared for PGA = 0.80g. Figure 15(A) shows that the SW-CBs specimen exhibited larger acceleration responses than the SW-RCBs specimen on most stories under the three sets of seismic excitations.

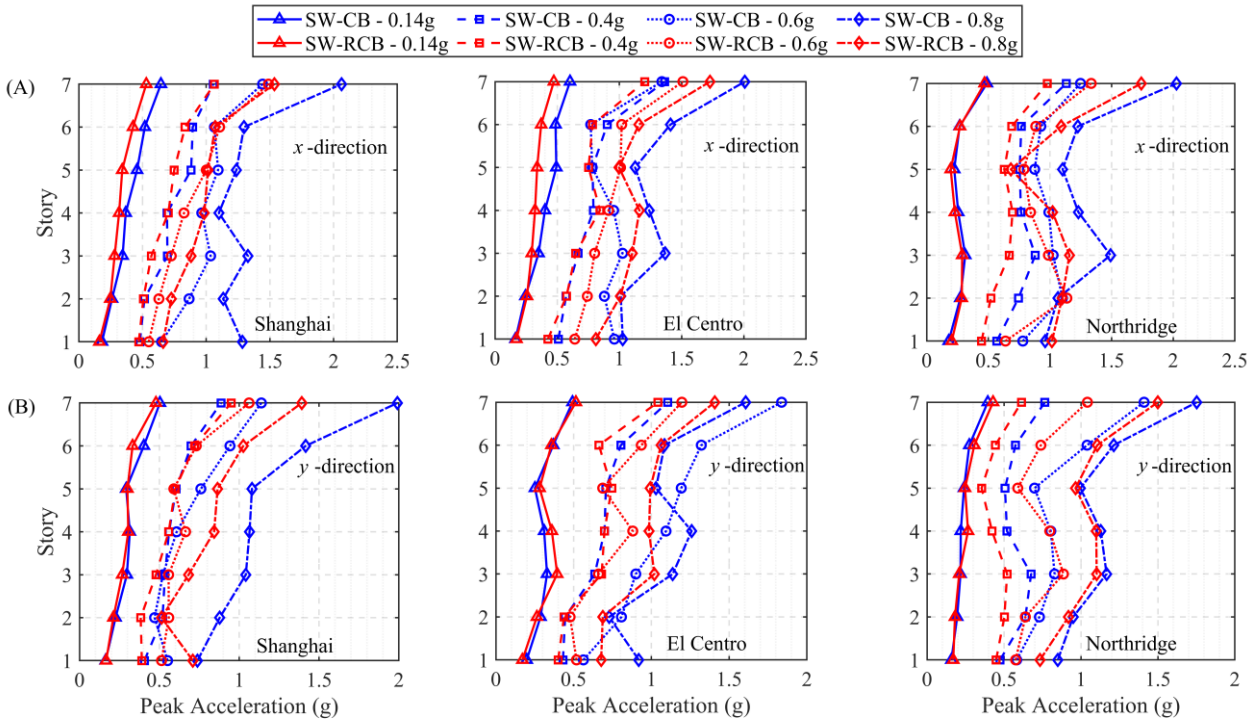


**FIGURE 15** Peak story accelerations along with the height of the SW-CBs and SW-RCBs for the three seismic excitations and each seismic intensity level: (A) *x*- and (B) *y*-direction.

*5.4 Story shear response*

Figure 16 compares the peak story shear along with the height of both specimens for the *x*- and *y*-direction. The shear force for each floor is obtained by multiplying the acceleration of that floor by its corresponding mass. The shear force for a particular floor is then determined as the sum of shear forces from all floors above it [58]. The results of the Shanghai earthquake are shown in this plot for the sake of brevity. The story shear forces of SW-RCBs were smaller than those of SW-CBs, especially in the *y*-direction due to the significant reduction in structural frequencies compared to the conventional structure, with a maximum difference of 41.60% occurring at *y*-direction under the PGA of 0.80g.

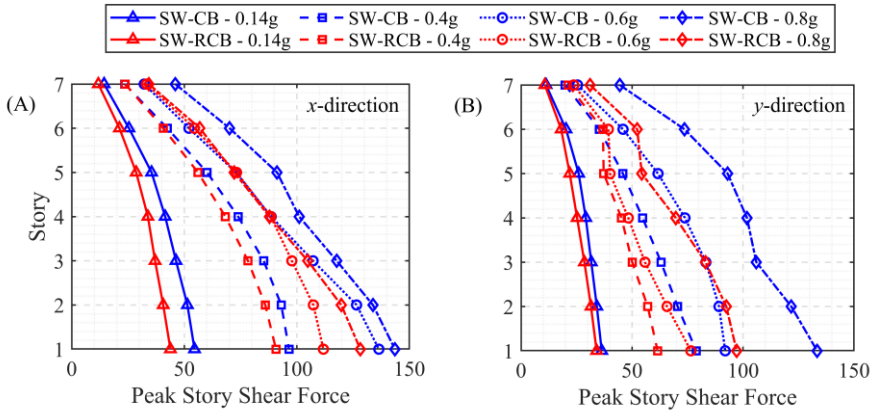


**FIGURE 16** Peak story shear along with the height of the SW-CBs and SW-RCBs for the Shanghai seismic excitations and each seismic intensity level: (A) *x*- and (B) *y*-direction.

*5.5 Strain response*

Figure 17 compares the peak strains measured CBs and RCBs' longitudinal rebars along with the height of both specimens for the *x*-direction. Results in the *y*-direction are not included for the sake of brevity. These results were measured by the strain gauge illustrated in Figure 6(C). The strain gauge was damaged during the construction or the experimental process in the sixth story in SW-CBs specimen and some positions in SW-RCBs; therefore, some results are omitted in the figures. However, the figures allow showing the overall trend. The strains of the measured longitudinal rebars in SW-RCBs were

considerably lower than those in SW-CBs, especially on the second and third stories, demonstrating that the deformation was concentrated in the hybrid device at mid-span of the RCBs. The rotational deformation and the severe concrete damage at the beam end could be effectively controlled and prevented.

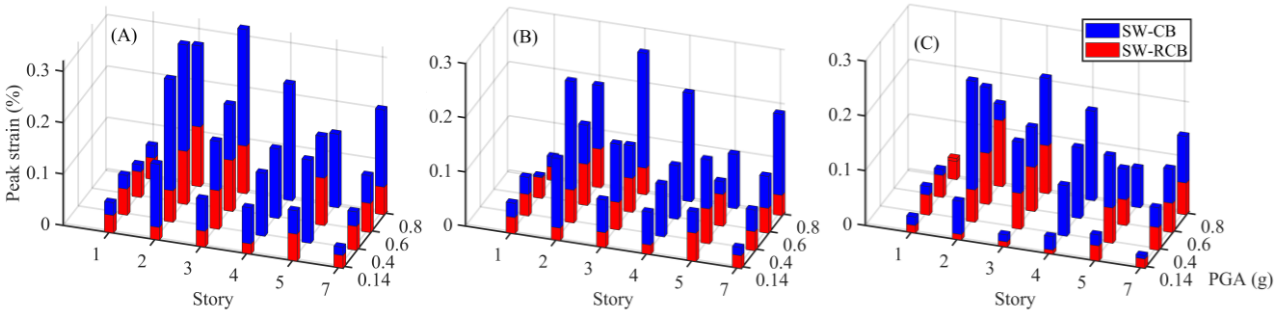


**FIGURE 17** Peak strains in the rebars of the CBs/RCBs in *x*-direction long with the height of the SW-CBs and SW-RCBs for the (A) Shanghai; (B) El Centro; and (C) Northridge seismic excitations and each seismic intensity level.

### *5.6 Additional tests of the SW-RCBs specimen with larger PGAs*

No obvious failure was observed in the SW-RCBs specimen under the three sets of records with PGA = 0.80g. For this reason, further tests were performed on the SW-RCBs with larger PGA = 1.04g, 1.24g, and 1.40g. Figure 18 shows the response histories of the rotations of the devices in the RCBs in the *x*-direction under the Shanghai earthquake for PGAs = 0.80g and 1.40g. It can be observed that the rotations at the second and third stories were relatively larger than the others, which is in accordance with the observed interstory drift distribution along with the high of the structures. At these stories, the rotations reached maximum values of approximately 0.030 rads and 0.080 rads, respectively, for the records with PGAs = 0.80g and 1.40g. For this largest records, all of the devices in the *x*-direction reached their peak strength but with rotations lower than the failure rotation limit of 0.085 rads according to the tests performed on the isolated components.

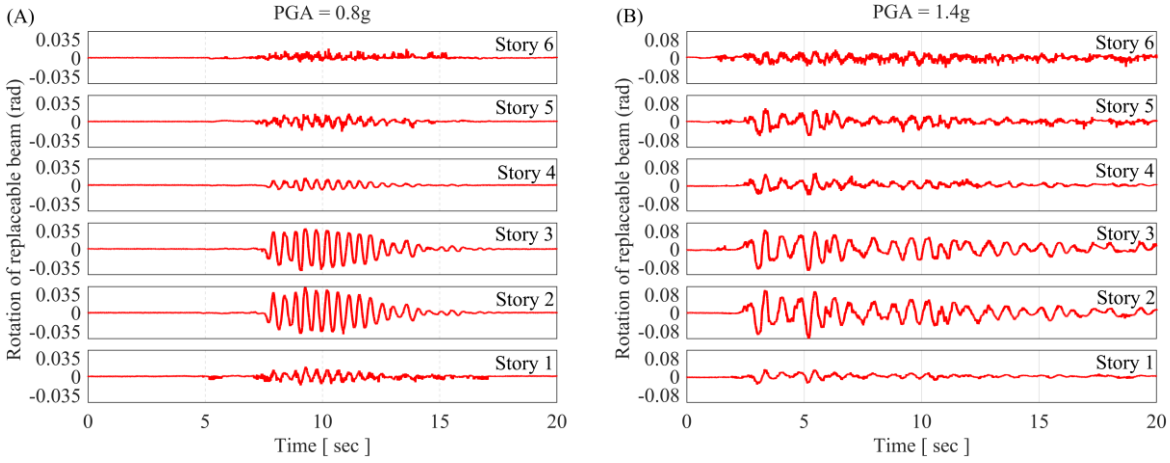


**FIGURE 18** The response history of the rotations of the replaceable devices in the *x*-direction under Shanghai artificial excitation: (A) with PGA of 0.80g; (B) with PGA of 1.40g.

## 6. FINITE ELEMENT (FE) MODELING AND SIMULATIONS

### *6.1 Finite Element (FE) Models*

3D finite element (FE) models of the tested structures were developed in OpenSees [52] and validated against the experimental results. Figure 19 provides an overview of the modeling strategy showing only one SW in the *x*-direction.

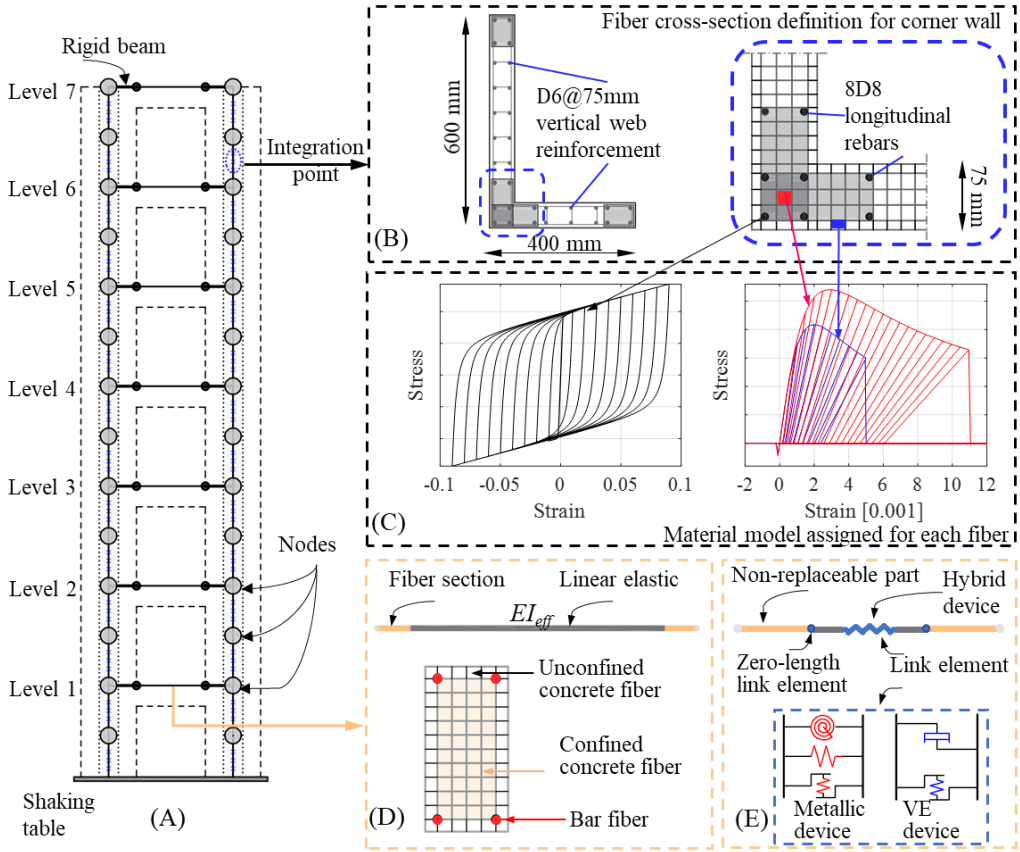


**FIGURE 19** Modeling approach and details for the coupled shear wall system (A) Finite element model; (B) cross-section of the corner wall with different levels of confinement of concrete; (C) Uniaxial constitutive laws for unconfined and confined concrete and steel reinforcement; (D) Beam with hinges element for coupling beam; (E) Non-linear model for RCB.

The FE models are composed of the RC SW piers and the coupling beams [Figure 19(A)]. The RC SW piers were modeled by L-shaped fiber sections employing force-based distributed-plasticity beam-column elements (*i.e., 'Force-Based Beam-Column'*) [52] [Figure 19(B)], each with four integration points. Two elements in series were used to simulate the RC SW piers at each story. The fiber section of the RC SW piers was divided into several parts including: *1)* the unconfined concrete cover; *2)* the stirrup-confined concrete in the different levels of confinement of boundary concrete; and *3)* the reinforcing steel. The Giuffre-Menegotto-Pinto constitutive model (*i.e., 'Steel02'*) [52] and Popovics Concrete Material (*i.e., 'Concrete04'*) [52] were adopted to simulate the stress-strain relationship of the reinforcing steel and concrete material, respectively, as shown in Figure 19(C). The gravity loads and seismic masses were uniformly applied at the four nodes at the edges of the SWs system of each story. Rigid diaphragms and fixed bases were adopted for the models of both structures. The rigid diaphragms were modeled by multi-point constraints applied at the nodes of each story (*i.e., 'RigidDiaphragm'*) [52]. The Rayleigh damping model based on tangent stiffness was used for the simulation. A variant stiffness matrix was considered and updated at each analysis time step. The values of the combination of mass and stiffness-proportional damping matrices were evaluated for a damping factor of 5% for the first six vibration modes.

For the SW-CBs, the CBs were slender and reinforced by the stirrups in a conventional method, and the plastic hinges observed in the tests indicated a typical flexural failure mode. Therefore, CBs were modeled by a distributed plasticity approach using the *'beamWithHinges'* elements in OpenSees [52] and two equivalent plastic hinge [59] was considered at two ends of the element. The fiber discretization of the rectangular section of the CBs included unconfined and confined concrete and steel rebar fibers [Figure 19(D)].

For the SW-RCBs, the modeling of the RCBs was slightly more complex. The non-replaceable beam segment was modeled by displacement-based fiber beam-column elements (*i.e., 'Displacement-Based Beam-Column'*) in OpenSees [52]. The hybrid device was modeled by using link elements working in parallel and simulating the responses of the metallic and viscoelastic devices. Additionally, zero-length shear springs were included between the beam and link elements to account for the shear deformability of the non-replaceable beam segments [Figure 19(E)].

The metallic device was modeled by a combination of shear, axial, and flexural links [Figure 19(E)]. The axial and flexural behavior of the metallic device were characterized by the *'Elastic'* material model in OpenSees [52] with stiffness

equal to $E_mA_m/L_{HD}$ and $E_mI_m/L_{HD}$, respectively. Conversely, the shear link was modeled by the *'Steel02'* material in OpenSees [52], with an initial stiffness ($K_m$) and a yielding force ($V_{m,y}$) of the metallic device defined according to the following equations:

$$K_m = \frac{1}{{L_{HD}}^3/(12E_mI_m)+L_{HD}/(G_mA_{m,w})} \quad ; \quad V_{m,y} = 0.6f_{m,yw}A_{m,w} \tag{7}$$

where $A_{m,w}$ is the sectional area of the web of the metallic device, and $f_{m,yw}$ is the yield stress of web material. The post-yield stiffness is assumed to be 1 % of the initial elastic stiffness.

The Kelvin-Voigt model [33] was used to simulate the mechanical properties of the viscoelastic device in the numerical simulation. The force in the viscoelastic device was defined by the expressions $F = Ku + C\dot{u}$, where $F$ is the device force; $u$ is the device deformation; $\dot{u}$ is the deformation rate; $K$ denotes the stiffness value of the spring element, and $C$ is the damping coefficient of the viscous element. The Kelvin-Voigt model was implemented by the parallel connection of the Maxwell (*i.e., 'ViscousDamper'*) material and an *'Elastic'* material with an elastic stiffness $k_1$ in OpenSees [52]. In the Maxwell model, the parameters $k_0$, $C_d$ and $\alpha$ control the elastic stiffness of linear spring, damping coefficient and velocity coefficient connected in series. The parameters of the viscoelastic device were calibrated against experimental results considering different deformation amplitudes. Figure 20 illustrates the comparison between the force-displacement responses from a component test and the numerical results showing a good agreement of the results.

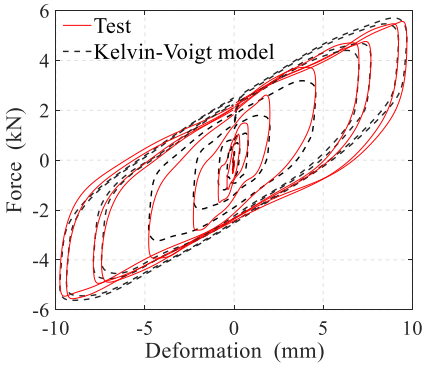


**FIGURE 20** Comparisons between recorded and identified hysteretic loops for viscoelastic devices under various strains.

### *6.2 Validation of the Finite Element (FE) Models against the experimental results*

Table 5 compares the natural frequencies for the first mode during Tests 1, 8, 15, 22, and 29 (see Table 4) evaluated from the experimental results and the numerical simulations, showing a good agreement. Similarly, Figure 21 and Figure 22 compare the experimental and numerical top story displacements for both the SW-CBs and SW-RCBs for several tests, including different records and intensities. Also in this case, the comparison shows a good agreement between the numerical and experimental results.

**TABLE 5** Comparison of the natural frequencies of the first mode.

| Test | 1 | | 8 | | 15 | | 22 | | 29 | |
|---|---|---|---|---|---|---|---|---|---|---|
| | SW-CBs | SW-RCBs | SW-CBs | SW-RCBs | SW-CBs | SW-RCBs | SW-CBs | SW-RCBs | SW-CBs | SW-RCBs |
| Exp (Hz) | 4.625 | 4.125 | 2.875 | 3.250 | 1.750 | 2.375 | 1.500 | 2.000 | 1.375 | 1.875 |
| Sim (Hz) | 4.528 | 4.129 | 2.878 | 3.408 | 1.874 | 2.718 | 1.703 | 2.443 | 1.370 | 2.154 |
| Ratio | 0.979 | 1.001 | 1.001 | 1.049 | 1.071 | 1.144 | 1.135 | 1.222 | 0.996 | 1.149 |

**Notes**: Exp represents the experimental result; Sim represents the simulation result; and Ratio represents the ratio between the simulation and experimental results.

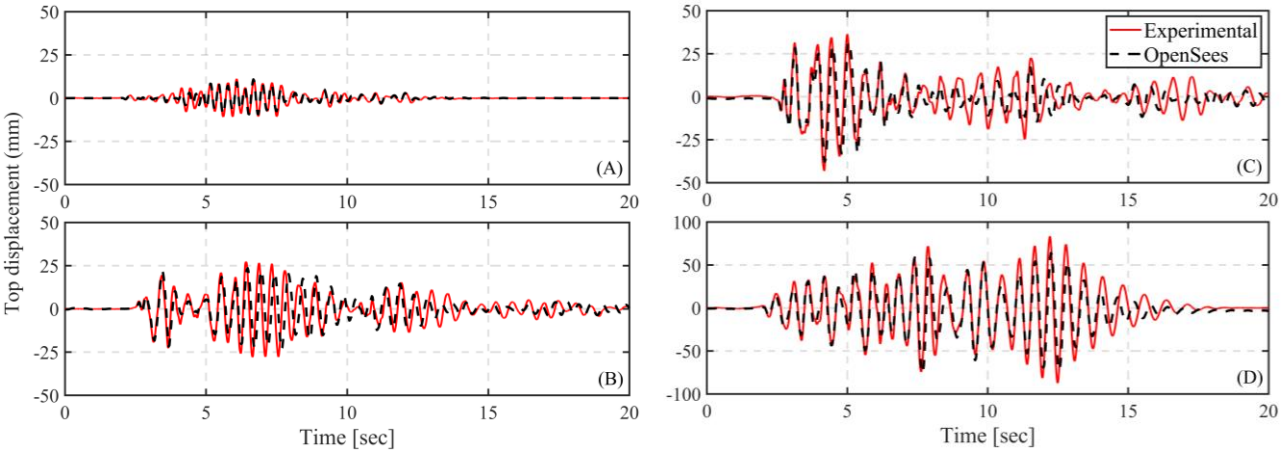


**FIGURE 21** Comparison of the experimental and numerical in OpenSees for the displacement response histories of SW-CBs in the *x*-direction at the roof level: (A) under Case 2: Shanghai 0.14g; (B) under Case 12: El Centro 0.40g; (C) under Case 18: El Centro 0.60g ; (D) under Case 23: Shanghai 0.8g.

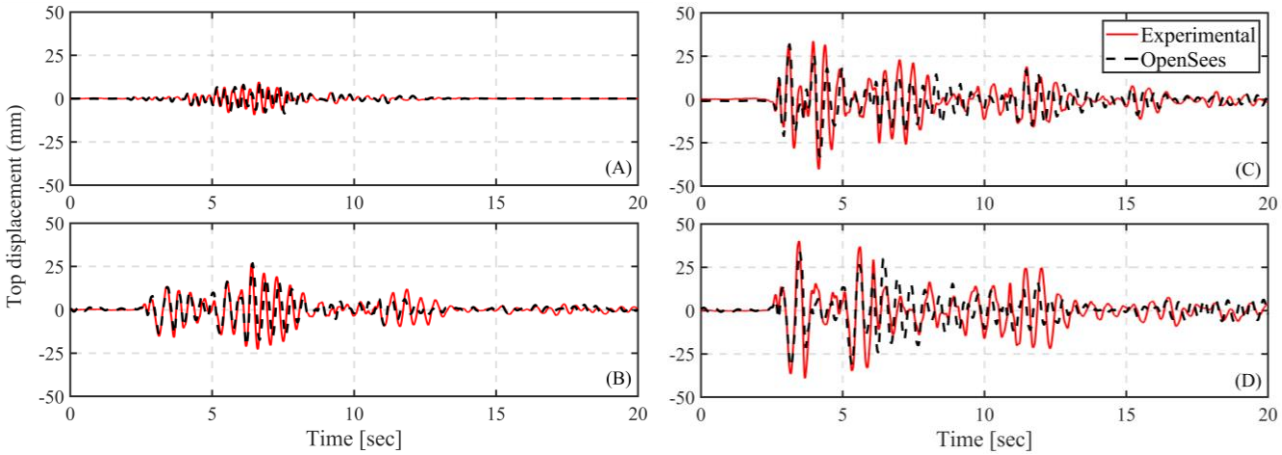


**FIGURE 22** Comparison of the experimental and numerical in OpenSees for the displacement response histories of SW-RCBs in the *x*-direction at the roof level: (A) under Case 2: Shanghai 0.14g; (B) under Case 12: El Centro 0.40g; (C) under Case 18: El Centro 0.60g ; (D) under Case 25: El Centro 0.80g.

*6.3 Parametric study*

The parametric numerical study was performed to investigate the influence of the distribution of the shear force between the metallic and viscoelastic devices (*i.e.*, the parameters $\psi = V_m/V_{HD}$ and $\chi = V_{ve}/V_{HD}$ defined in Section 2.2) on the seismic response of the SW-RCBs. In addition to the equally distribution of the ratios $\psi = \chi = 0.5$, the ratios $\psi$ were set to 0.3, 0.4, 0.6, and 0.7, and the corresponding ratios $\chi$ were adjusted to 0.7, 0.6, 0.4, and 0.3 to maintain the total shear force in the hybrid device unchanged. It is noteworthy that the initial stiffness of the devices was kept unchanged in order to keep constant the natural period of the structure. Five configurations of the hybrid device were considered and referred to as SW-RCB-hA to hE with the modeling parameters reported in Table 6 and defined in Section 2.2. The modeling parameters for the viscoelastic device in the SW-RCB-hC configuration were calibrated against the test results as discussed in Section 2.1. The response of the viscoelastic devices in other configurations were achieved by adjusting the damping coefficient $C_d$ to obtain the desired shear force under peak deformation. The shear stiffness and the yielding strength of the metallic device were calibrated based on the configuration according to the Equation (7). Figure 23(A) and (B) show the cyclic response of the metallic and viscoelastic devices for the SW-RCB-hA to hE respectively for small and large deformations.

**TABLE 6** Design results and modeling parameters for different configured hybrid devices in the innovation structure.

| | $\psi = V_m/V_{HD}$ | $\chi = V_{ve}/V_{HD}$ | $V_m$ (N) | $V_{ve}$ (N) | $k_0$ (N/m) | $C_d$ | $\alpha$ | $k_1$ (N/m) |
|---|---|---|---|---|---|---|---|---|
| SW-RCB-hA | 0.3 | 0.7 | 3600 | 8400 | $8.50\times10^6$ | $0.55\times10^4$ | 0.4218 | $4.49\times10^5$ |
| SW-RCB-hB | 0.4 | 0.6 | 4800 | 7200 | $8.50\times10^6$ | $1.19\times10^4$ | 0.4218 | $4.49\times10^5$ |
| SW-RCB-hC | 0.5 | 0.5 | 6000 | 6000 | $8.50\times10^6$ | $1.75\times10^4$ | 0.4218 | $4.49\times10^5$ |
| SW-RCB-hD | 0.6 | 0.4 | 7200 | 4800 | $8.50\times10^6$ | $2.29\times10^4$ | 0.4218 | $4.49\times10^5$ |
| SW-RCB-hE | 0.7 | 0.3 | 8400 | 3600 | $8.50\times10^6$ | $2.80\times10^4$ | 0.4218 | $4.49\times10^5$ |

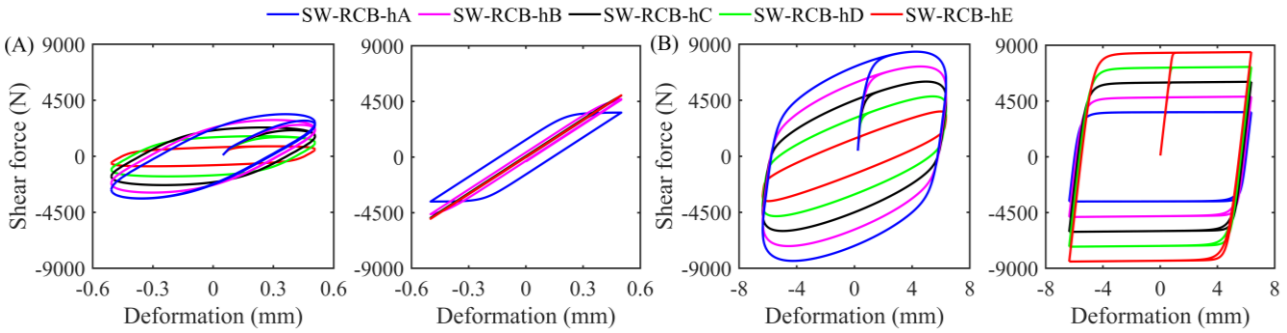


**FIGURE 23** Hysteresis behavior of metallic and viscoelastic devices for configurations SW-RCB-hA to hE: (A) small deformations under frequent earthquakes; and (B) large deformations under rare earthquakes.

A set of 22 far-field ground motion records adopted by the FEMA P695 [60] was selected to perform non-linear response history analyses of the SW-RCBs considering different configurations of the hybrid device and accounting for the record-to-record variability. Individual ground motions records were normalized and scaled to the 'frequent' (*i.e.,* probability of exceedance of 63% in 50 years), 'moderate' (*i.e.,* probability of exceedance of 10% in 50 years), and 'rare' earthquake intensity (*i.e.,* probability of exceedance of 2% in 50 years) as defined in the Chinese code [2].

Figure 24 and Figure 25 compare the peak interstory drifts and peak story acceleration along with the height of the SW-RCBs under the 'frequent', 'moderate', and 'rare' earthquake intensity. The solid lines and dashed lines represent the mean response from the 22 ground motions and the mean response plus the standard deviation for the five different configurations, respectively.

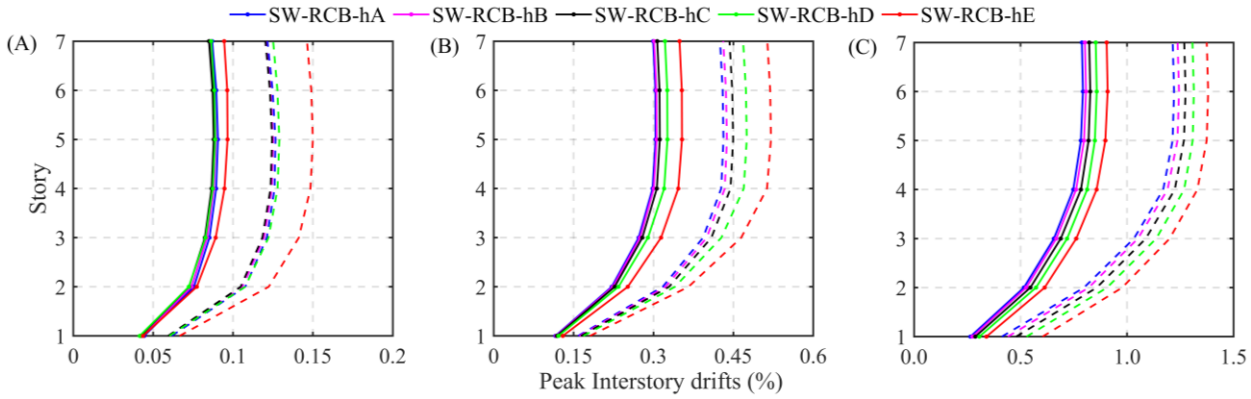


**FIGURE 24** Peak Interstory drift ratios along with the height of the SW-RCBs specimens with different hybrid device configurations: (A) 'frequent'; (B) 'moderate'; and (C) 'rare' earthquake intensity.

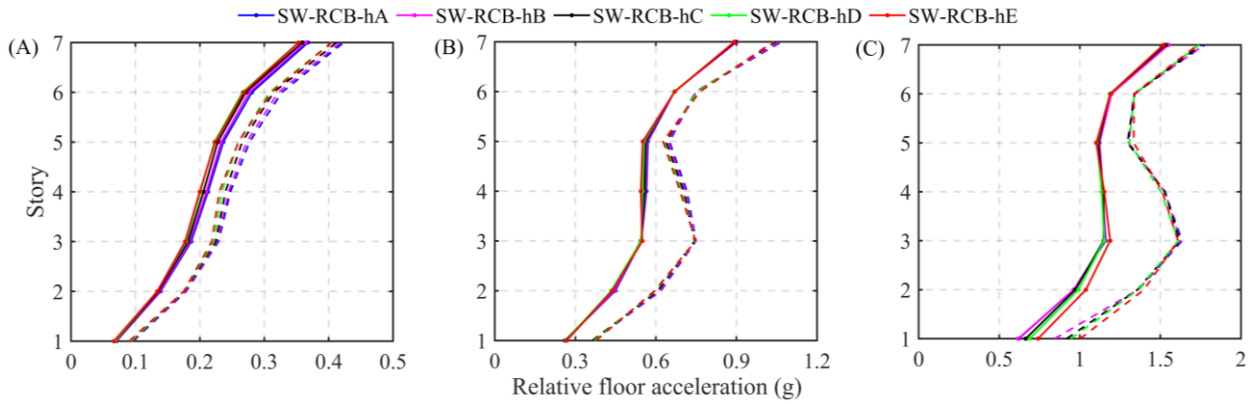


**FIGURE 25** Peak story accelerations along with the height of the SW-RCBs specimens with different hybrid device configurations: (A) 'frequent'; (B) 'moderate'; and (C) 'rare' earthquake intensity.

The results show that the IDRs of the SW-RCBs decrease for increasing values of the $\chi$ ratio, with differences between the smallest and the largest $\chi$ ratios reaching up to 9.00%, 14.06% and 12.78% under the 'frequent', 'moderate' and 'rare' earthquake intensities, respectively. As shown in Figure 24, the SW-RCB-hE configuration exhibits the largest IDRs for

the three seismic input intensities. This is due to the fact that the metallic devices in this configuration have the highest yielding force and hence, they need large deformations to start dissipating the seismic energy. At the same time, the energy dissipation in viscoelastic device is decreased due to the reduced damping coefficient. However, it can be inferred from the very similar responses exhibited by the SW-RCB-hA and SW-RCB-hB configurations that the reduction in IDRs is limited as the yielding shear force of the metallic device decreases. In terms of peak accelerations the results show smaller differences among the five configurations reaching up to 3.92%, 1.00% and 2.08%, under the 'frequent', 'moderate' and 'rare' earthquake intensities, respectively.

In general, the results of this parametric study show the beneficial effects in terms of IDRs reduction obtained by considering larger $\chi$ ratios (*i.e.,* a larger contribution of the viscoelastic device to the shear force). However, some additional considerations are required. In fact, setting a larger $\chi$ ratio implies reducing the contribution of the metallic device (*i.e.,* lower $\psi$ ratio) which significantly control the stiffness of the structure and are independent from the vibrations frequency. Therefore, too low $\psi$ ratios could result in unrealistic designs of the metallic devices and/or to an inadequate stiffness during 'frequent' earthquakes or wind loads. The optimization of the $\psi$ and $\chi$ ratios should consider stiffness, strength, and structural response, etc. by using the complex optimization algorithms which is beyond the scope of the present paper.

## 7. CONCLUSIONS

The present study experimentally and numerically investigates an innovative reinforced concrete (RC) shear wall (SW) structure with replaceable coupling beams (RCBs) equipped with hybrid devices. These hybrid devices couples metallic and viscoelastic dampers and aim at satisfying multiple lateral load performances effectively. The seismic performance of the proposed system is investigated through a series of shaking table tests on two 1/4-scale seven-story SW structure specimens: one with conventional RC coupling beams (SW-CBs) and the other with innovative hybrid RCBs (SW-RCBs). The experimental tests highlighted the advantages of the SW-RCBs with respect to the SW-CBs. In particular, the following observations could be summarized: *1)* the initial elastic lateral stiffness of the SW-CBs and SW-RCBs specimens was similar but their failure modes and damage evolution were significantly different; *2)* the SW-CBs experienced significant damage in the coupling beams and, for higher intensities the concrete cover crushed, the reinforcement were exposed and plastic hinges generated at the connection between the CBs and the SW. Conversely, the SW-RCBs showed a limited damage and mainly concentrated in the hybrid devices of the RCBs. This is also demonstrated by the lower strain measured in the longitudinal rebars of the coupling beams. These tests observations suggest that the SW-RCBs could be easily repaired, resulting in reduced downtime in the aftermath of 'rare' (high-intensity) earthquakes; *3)* the interstory drift ratios, accelerations and story shear forces were reduced in the SW-RCBs, for the whole range of seismic intensities investigated. For small seismic intensities the benefit of using the SW-RCBs were limited. Conversely, significant benefits were observed for high-intensity earthquakes due to the limited damage experienced by the SW-RCBs compared to SW-CBs; *4)* in some cases the top displacement response of the SW-RCBs was slightly larger for 'frequent' earthquake due to the lower stiffness of the RCBs compared to the conventional CBs. This was due to the slightly lower stiffness of the RCBs with respect to the CBs. Additionally, 3D finite element models for the shaking table test specimens were developed in OpenSees and validated against experimental results. Successively, a numerical parametric study based on non-linear response history analyses under a set of 22 ground motions scaled to different intensities was performed to provide some insights on the influence of different design configurations of the hybrid device on the peak interstory drifts and peak story accelerations. In particular, this part of the study focused on investigating the influence of the distribution of the shear force between the metallic and viscoelastic devices on the seismic response of the SW-RCBs. The results show that the peak interstory drifts is more sensitive to the shear distribution in the hybrid device compared to story acceleration response. Moreover, the results show the beneficial effects provided by a larger contribution of the viscoelastic device in limiting the interstory drifts. Additional studies investigating optimal shear force distribution between the metallic and the viscoelastic device considering the structural stiffness, strength and ductility are required to develop clear design recommendations for the proposed structural system. Moreover, additional considerations are required to explicitly investigate the performance of the structure under wind-induced vibrations.

## ACKNOWLEDGEMENTS

The financial support provided by the Natural Key R&D Program of China (2018YFC0705602) is greatly appreciated by the authors. The first author also gratefully acknowledges the China Scholarship Council (Grant No. 202006260212) for financial support for the research visit at UCL.

## REFERENCES

1. European Committee for Standardization (CEN). EN 1998-1:2004 Eurocode 8: Design of Structures for Earthquake Resistance - Part 1: General Rules, Seismic Actions and Rules for Buildings. In:2005.
2. GB 50011-2010. Code for seismic design of buildings. In. Beijing: China Architecture and Industry Press; 2010.

3. American Society of Civil Engineers. ASCE/SEI 7-16 Minimum Design Loads and Associated Criteria for Buildings and Other Structures. In:2017.
4. Cimellaro GP, Dueñas-Osorio L, Reinhorn AM. Special Issue on Resilience-Based Analysis and Design of Structures and Infrastructure Systems. *Journal of Structural Engineering.* 2016;142(8):C2016001.
5. Freddi F, Galasso C, Cremen G, Dall'Asta A, Di Sarno L, Giaralis A, Gutiérrez-Urzúa F, Málaga-Chuquitaype C, Mitoulis SA, Petrone C, Sextos A, Sousa L, Tarbali K, Tubaldi E, Wardman J, Woo G. Innovations in earthquake risk reduction for resilience: Recent advances and challenges. *International Journal of Disaster Risk Reduction.* 2021;60:102267.
6. Soong TT, Spencer BF. Supplemental energy dissipation: state-of-the-art and state-of-the-practice. *Engineering Structures.* 2002;24(3):243-259.
7. Symans MD, Charney FA, Whittaker AS, Constantinou MC, Kircher CA, Johnson MW, McNamara RJ. Energy Dissipation Systems for Seismic Applications: Current Practice and Recent Developments. *Journal of Structural Engineering.* 2008;134(1):3-21.
8. Gutiérrez-Urzúa F, Freddi F. Influence of the design objectives on the seismic performance of steel moment resisting frames retrofitted with buckling restrained braces. *Earthquake Engineering & Structural Dynamics.* 2022;51(13):3131-3153.
9. Lu X, Chen Y, Jiang H. Earthquake Resilience of Reinforced Concrete Structural Walls with Replaceable "Fuses". *Journal of Earthquake Engineering.* 2018;22(5):801-825.
10. Calvi PM, Calvi GM. Historical development of friction-based seismic isolation systems. *Soil Dynamics and Earthquake Engineering.* 2018;106:14-30.
11. Dall'Asta A, Leoni G, Gioiella L, Micozzi F, Ragni L, Morici M, Scozzese F, Zona A. Push-and-release tests of a steel building with hybrid base isolation. *Engineering Structures.* 2022;272:114971.
12. Tong F, Christopoulos C. Uncoupled rocking and shear base-mechanisms for resilient reinforced concrete high-rise buildings. *Earthquake Engineering & Structural Dynamics.* 2020;49(10):981-1006.
13. Freddi F, Dimopoulos CA, Karavasilis TL. Experimental Evaluation of a Rocking Damage-Free Steel Column Base with Friction Devices. *Journal of Structural Engineering.* 2020;146(10):04020217.
14. Shen Y, Freddi F, Li Y, Li J. Parametric experimental investigation of unbonded post-tensioned reinforced concrete bridge piers under cyclic loading. *Earthquake Engineering & Structural Dynamics.* 2022;51(15):3479-3504.
15. Elettore E, Freddi F, Latour M, Rizzano G. Design and analysis of a seismic resilient steel moment resisting frame equipped with damage-free self-centering column bases. *Journal of Constructional Steel Research.* 2021;179:106543.
16. Pieroni L, Freddi F, Latour M. Effective placement of self-centering damage-free connections for seismic-resilient steel moment resisting frames. *Earthquake Engineering & Structural Dynamics.* 2022;51(5):1292-1316.
17. Li J, Wang W, Cao Z. Self-centering hybrid dampers for improving seismic resilience. *Engineering Structures.* 2021;244:112829.
18. Shen Y, Liu X, Li Y, Li J. Cyclic tests of precast post-tensioned concrete filled steel tubular (PCFT) columns with internal energy-dissipating bars. *Engineering Structures.* 2021;229:111651.
19. El-Tawil S, Harries KA, Fortney PJ, Shahrooz BM, Kurama Y. Seismic Design of Hybrid Coupled Wall Systems: State of the Art. *Journal of Structural Engineering.* 2010;136(7):755-769.
20. Mahin SA, Bertero VV. Nonlinear Seismic Response of a Coupled Wall System. *Journal of the Structural Division.* 1976;102(9):1759-1780.
21. Yayong W. Lessons learned from the 5.12 Wenchuan Earthquake: evaluation of earthquake performance objectives and the importance of seismic conceptual design principles. *Earrhq Eng Eng Vib.* 2008;7(3):255-262.
22. Murat S, Dan P, Ahmed G, Denis M, Rob S, Perry A, Robert T, Carlos V, Hanping H. Performance of reinforced concrete buildings during the 27 February 2010 Maule (Chile) earthquake. *Canadian Journal of Civil Engineering.* 2013;40(8):693-710.
23. Jünemann R, de la Llera JC, Hube MA, Vásquez JA, Chacón MF. Study of the damage of reinforced concrete shear walls during the 2010 Chile earthquake. *Earthquake Engineering & Structural Dynamics.* 2016;45(10):1621-1641.
24. Kam WY, Pampanin S. The seismic performance of RC buildings in the 22 February 2011 Christchurch earthquake. *Structural Concrete.* 2011;12(4):223-233.
25. Wilkinson S, Grant D, Williams E, Paganoni S, Fraser S, Boon D, Mason A, Free M. Observations and implications of damage from the magnitude Mw 6.3 Christchurch, New Zealand earthquake of 22 February 2011. *Bulletin of Earthquake Engineering.* 2013;11(1):107-140.
26. Fortney PJ, Shahrooz BM, Rassati GA. Large-Scale Testing of a Replaceable "Fuse" Steel Coupling Beam. *Journal of Structural Engineering.* 2007;133(12):1801-1807.
27. Ji X, Liu D, Sun Y, Molina Hutt C. Seismic performance assessment of a hybrid coupled wall system with replaceable steel coupling beams versus traditional RC coupling beams. *Earthquake Engineering & Structural Dynamics.* 2017;46(4):517-535.
28. Jun T, Botao M, Weihua L, Hao Z, Dongxue C. Pseudo-static test for coupling beam damper of coupled shear wall structure. *Journal of Building Structures.* 2010;31(12):92.

29. Chen Y, Lu X. New replaceable coupling beams for shear wall structures. Paper presented at: 15th World Conference on Earthquake Engineering2012.
30. Chung H-S, Moon B-W, Lee S-K, Park J-H, Min K-W. Seismic performance of friction dampers using flexure of rc shear wall system. *The Structural Design of Tall and Special Buildings.* 2009;18(7):807-822.
31. Qu Z, Ji X, Shi X, Wang Y, Liu H. Cyclic loading test of steel coupling beams with mid-span friction dampers and RC slabs. *Engineering Structures.* 2020;203:109876.
32. Lettieri A, de la Peña A, Freddi F, Latour M. Damage-free self-centring links for eccentrically braced frames: development and numerical study. *Journal of Constructional Steel Research.* 2023;201:107727.
33. Christopoulos C, Montgomery M. Viscoelastic coupling dampers (VCDs) for enhanced wind and seismic performance of high-rise buildings. *Earthquake Engineering & Structural Dynamics.* 2013;42(15):2217-2233.
34. Montgomery M, Christopoulos C. Experimental Validation of Viscoelastic Coupling Dampers for Enhanced Dynamic Performance of High-Rise Buildings. *Journal of Structural Engineering.* 2015;141(5):04014145.
35. Tubaldi E, Ragni L, Dall'Asta A, Ahmadi H, Muhr A. Stress softening behaviour of HDNR bearings: modelling and influence on the seismic response of isolated structures. *Earthquake Engineering & Structural Dynamics.* 2017;46(12):2033-2054.
36. Kim YC, Kanda J. Wind response characteristics for habitability of tall buildings in Japan. *The Structural Design of Tall and Special Buildings.* 2008;17(3):683-718.
37. Burton MD, Kwok KC, Abdelrazaq A. Wind-induced motion of tall buildings: designing for occupant comfort. *International Journal of High-Rise Buildings.* 2015;4(1):1-8.
38. Irwin PA. Wind engineering challenges of the new generation of super-tall buildings. *Journal of Wind Engineering and Industrial Aerodynamics.* 2009;97(7):328-334.
39. Ibrahim YE, Marshall J, Charney FA. A visco-plastic device for seismic protection of structures. *Journal of Constructional Steel Research.* 2007;63(11):1515-1528.
40. Karavasilis TL, Blakeborough T, Williams MS. Development of nonlinear analytical model and seismic analyses of a steel frame with self-centering devices and viscoelastic dampers. *Computers & Structures.* 2011;89(11):1232-1240.
41. Vargas R, Bruneau M. Effect of Supplemental Viscous Damping on the Seismic Response of Structural Systems with Metallic Dampers. *Journal of Structural Engineering.* 2007;133(10):1434-1444.
42. Marshall JD, Charney FA. Seismic response of steel frame structures with hybrid passive control systems. *Earthquake Engineering & Structural Dynamics.* 2012;41(4):715-733.
43. Rahnavard R, Rebelo C, Craveiro HD, Napolitano R. Numerical investigation of the cyclic performance of reinforced concrete frames equipped with a combination of a rubber core and a U-shaped metallic damper. *Engineering Structures.* 2020;225:111307.
44. Marshall JD, Charney FA. A hybrid passive control device for steel structures, I: Development and analysis. *Journal of Constructional Steel Research.* 2010;66(10):1278-1286.
45. Marshall JD, Charney FA. A hybrid passive control device for steel structures, II: Physical testing. *Journal of Constructional Steel Research.* 2010;66(10):1287-1294.
46. Yamamoto M, Sone T. Damping systems that are effective over a wide range of displacement amplitudes using metallic yielding component and viscoelastic damper in series. *Earthquake Engineering & Structural Dynamics.* 2014;43(14):2097-2114.
47. Benavent-Climent A, Escolano-Margarit D, Yurkin Y, Ponce-Parra H, Arcos-Espada J. Shake table tests on a reinforced concrete waffle-flat plate structure with new hybrid energy dissipation devices. *Earthquake Engineering & Structural Dynamics.* 2022;n/a(n/a).
48. Oh SH, Choi KY, Kim H-J, Kang CH. Experimental validation on dynamic response of RC shear wall systems coupled with hybrid energy dissipative devices. 15WCEE; 2012; Lisbon, Portugal.
49. Li S, Jiang H, He L. Study of a new type of replaceable coupling beam in reinforced concrete shear wall structures. *The Structural Design of Tall and Special Buildings.* 2019;28(10):e1620.
50. Jiang H, Li S, Bolander JE, Kunnath SK. Seismic Performance of a New Type of Coupled Shear Wall with Replaceable Components: Experimental Validation. *Journal of Earthquake Engineering.* 2022:1-23.
51. Li S, Jiang H, Kunnath SK. Seismic assessment of a new resilient coupled shear wall. *Engineering Structures.* 2023;277:115476.
52. Mazzoni S, McKenna F, Scott MH, Fenves GL. OpenSEES, Open system for earthquake engineering simulation, Pacific earthquake engineering research Centre (PEER), Univ. of California, Berkley, CA, 2009, Available at: http://opensees.berkeley.edu.
53. GB 50010-2010. Code for design of concrete structures. In. Beijing: China Architecture and Industry Press; 2010.
54. Building code requirements for structural concrete (ACI 318-19) and commentary on building code requirements. American Concrete Institute, Farmington Hills, MI: ACI-318 (2019) Committee 318; 2019. . In.
55. ANSI/AISC. Seismic provisions for structural steel buildings. In. *AISC 341-10*. Chicago: IL: American Institute of Steel Construction.; 2010.
56. Technical specifications for concrete structures of tall buildings. 2010.
57. DGJ08-9-2013. Code for seismic design of buildings. In. Shanghai: Shanghai Urban and Rural Development and Transportation Commission; 2013.

58. Martinelli P, Filippou FC. Simulation of the shaking table test of a seven-story shear wall building. *Earthquake Engineering & Structural Dynamics.* 2009;38(5):587-607.
59. Wang Z, Pan W. A hybrid coupled wall system with replaceable steel coupling beams for high-rise modular buildings. *Journal of Building Engineering*. 2020;31:101355.
60. *Quantification of building seismic performance factors.* CA: FEMA P695; 2009.